Application of Data-Driven Modal Decomposition Techniques to the Non-Stationary Case of Scramjet Unstart

Undergraduate Honors Thesis

Jack Sullivan

A Thesis Presented in Partial Fulfillment of the Requirements for Graduation with Honors Distinction

Under the advisement of Professor Datta Gaitonde

Department of Mechanical and Aerospace Engineering

The Ohio State University

April, 2021

Abstract

Scramjets are a class of high-speed aerospace propulsion devices that operate with no moving parts and perform combustion at supersonic speeds. They offer a viable option for reusable, efficient, air-breathing hypersonic propulsion and they will be of critical importance to powering the transportation and defense systems of the future. Due to the lack of turbo-machinery in scramjet flow paths, sufficient compression and velocity reduction of the flow must be achieved using the Pre-Combustion Shock Train (PCST), which is a series of shocks in the isolator portion of a scramjet. Under certain conditions, the PCST is ejected out of the front of the engine, causing the engine to unstart. The consequences of unstart are severe, with the engine no longer producing thrust, and potentially causing complete vehicle loss. This work focuses on a high fidelity, computationally generated unstart simulation, in which a pressure induced unstart event is potentially controlled by an upstream cavity. Since such high-fidelity databases are large and difficult to analyze, modal decomposition techniques are often employed. The challenge in applying these techniques for the unstart problem is that it is not stationary i.e., it is unsteady but does not oscillate about a mean position. To address this, two data-driven modal decomposition techniques, Dynamic Mode Decomposition (DMD) and multi-resolution DMD (mrDMD) are examined by applying them to the streamwise component of the unstarting velocity field. The mrDMD algorithm was first validated on the statistically stationary case of supersonic flow over a wall-mounted turret before it was applied to the unstart problem. Results from the DMD analysis of unstart are compared to those from a 4-level mrDMD analysis, which allows for hierarchical time-frequency analysis. DMD was able to capture some gross flow features of the unstart event, such as final PCST location, top and bottom wall separation, and cavity shear layer oscillations. mrDMD was able to identify all of these features as well, and additionally was able to capture the PCST and separation bubbles in their correct spatio-temporal vicinities as the isolator flow-field evolved over time. DMD, and mrDMD to a lesser extent, exhibited difficulty in capturing the travelling shock waves of the PCST in a physically meaningful manner, which is likely due to the methods being based on the Singular Value Decomposition. It was shown that despite these difficulties in capturing moving waves, mrDMD clearly resolved spatio-temporal coherent structures in the isolator that DMD completely failed to. However, mrDMD may require the snapshots to have finer spatiotemporal resolution, to allow for more than the current 4-level analysis, to truly reveal its benefits, such as detecting and controlling unstart.

Acknowledgements

Above all, I would like to thank my advisor, Professor Datta Gaitonde, for affording me the opportunity to perform exciting, meaningful, and rewarding research as an undergraduate student. Over this past year, I've been able to change the way I approach science and engineering, expand my technical knowledge, and develop better communication skills, all thanks to the continual guidance and support of Professor Gaitonde. I am beyond excited to continue to work with him as I begin my graduate career.

I would also like to acknowledge the support I received from the many graduate students and post doctoral researchers throughout the course of my project. First and foremost, I would like thank Dr. Rajesh Ranjan for helping me gain a thorough understanding of mrDMD and modal decomposition techniques in general. Secondly, I need to thank Mikala Malkus for helping me navigate the same path she did, working as an undergraduate with the HFCMPL. Finally, countless thanks to all the other members of the HFCMPL for inspiring discussions, technical support, and general guidance. Also not enough can be said for how all members, Professor Gaitonde included, were still able to make an entirely virtual research process enriching and fun. Can't wait to meet you all.

Finally, I would like to extend thanks to my friends, family, and all others who have helped me reach my goals in life. Your support means the world.

Contents

List of Figures

Chapter 1: Introduction

1.1 Data Driven Modeling

Recent advances in both computational simulation techniques and experimental measurement methods have made the collection of high fidelity data sets more ubiquitous than ever before. As a result, dynamical systems can be accurately measured at an extremely high level of spatiotemporal detail. However, the collection of data at such a high level of detail can lead to extraordinarily large data sets, especially for modern systems of interest which are often highly complex. These large, high-dimensional data sets often become difficult to analyze and extract meaning from, simply due to their size. The field of data driven modeling offers a way to overcome this difficulty, by applying mathematical techniques that allow for meaningful quantification of the system's dynamics by characterizing and extracting underlying patterns in the data. Another exciting aspect of data driven modeling is that it represents an 'equation free' modeling technique, meaning no *a priori* knowledge of the equations that govern the dynamics is needed to successfully perform analysis of the system.

When looking at a given high-dimensional data set taken from a complex system, the data can appear disorganized and chaotic, especially if the system evolves in a non-linear fashion over time. However, the complex dynamics of a system often evolve according to some underlying low rank behavior that dominates the data set. For fluid dynamics problems, the low rank patterns that define the dynamical behavior of a data set correspond to spatiotemporal coherent flow structures. Accurate identification of a fluid system's low rank dynamics and dominant coherent structures can not only provide insight into the underlying physics of the system, but also allow for future state prediction and control development. To identify the important low-dimensional patterns from the full high-dimensional data set, modal decomposition techniques are employed. Data driven decomposition techniques such as Proper Orthogonal Decomposition (POD) and Dynamic Mode Decomposition (DMD) exist, while other decomposition techniques that are based on some operator relevant to the system in question, such as Koopman analysis, global linear stability analysis, and resolvent analysiscan also be employed [4]. While the presented work focuses on the data driven DMD method and its multi-resolution extension, it is important to note the underlying theory behind modal decomposition techniques as a whole.

The aforementioned modal decomposition methods, whether operator or data driven, allow for the identification of low-dimensional, dynamically dominant features present in a system. The application of these decomposition techniques allow for a low rank representation of the original system, by identifying the key dynamical features and ignoring those that are not as important. When applied to a fluid dynamics problem, these techniques can identify flow-features that dominate the system, such as shock-boundary layer interactions (SBLIs), shear

layer oscillations, and large scale turbulence, and the original complex flow-field can be modeled very efficiently using only the coherent structures that have large influence over the flow.

While all commonly used modal decomposition techniques have their respective advantages and disadvantages, the present work focuses solely on the DMD method and one of its extensions. DMD is an especially insightful decomposition technique since its algorithm not only allows for the identification of important coherent structures in a flow-field, but also gives some insight into how these modes evolve in time, which allows for a low-rank, efficient time reconstruction of the original dynamical system to be created. An additional benefit of DMD is that it is relatively easy to implement and computationally efficient, with the cost of the algorithm being a Singular Value Decomposition (SVD) of all but one of the snapshots in the database being considered. However, since the DMD algorithm breaks down the data set being analyzed into spatial modes with associated frequencies and growth/decay rates, DMD is best suited for systems with neutral, oscillatory dynamics, and care must be taken when applying the method to data sets that are taken from transient or unstable systems [5]. The subsequent sections outline the motivation for using an extension of DMD (called mrDMD) that is better suited for transient data sets, and frames how mrDMD is applied to the problem of scramjet unstart.

1.1.1 Dynamic Mode Decomposition

Dynamic Mode Decomposition combines aspects of spatial modal decomposition with the Fourier transform, allowing for the identification of coherent structures in a dynamical system and their associated time dynamics. The method was first introduced by Schmid et al in the fluids community in 2008 [6], and subsequently the most modern definition of the DMD method was formulated by Tu et al in 2013 [7]. Since DMD is a data driven method, the only input required is the raw data collected from a given experiment or simulation, that are organized into a time series of snapshots.

DMD is deeply connected with Koopman spectral theory as shown by Rowley et al in 2009 [8]. Koopman theory states that for any non-linear dynamical system there exists an infinite dimensional linear operator, called the Koopman operator, that exactly describes how the dynamics evolve in time. Within Koopman theory, the measurements of a dynamical system are taken as functions, and consequentially they form a Hilbert space where the infinite dimensional Koopman operator represents the action of the dynamical system [9]. In real world applications, a limit to dimensionality is introduced by taking measurements at a set of finite data points ($i = 1, 2, ...n$) over a finite time range ($t = 1, 2, ...m$), and an exact calculation of the Koopman operator cannot be obtained. However, the DMD method accurately computes a linear operator within the finite dimensional space spanned by the data set, that accurately approximates the infinite dimensional Koopman operator. Thus DMD represents a way to approximate the dynamics of a non-linear system through a finite-dimensional lin-

ear operator.

To successfully implement the DMD method, the dynamical system being examined is modeled as the differential equation,

$$\frac{d\mathbf{x}}{dt} = \mathcal{A}\mathbf{x} \tag{1}$$

Here, $\mathbf{x}$ represents the current state of the system and $\mathcal{A}$ represents the linear model of the continuous time dynamics. This form of differential equation can be solved with the eigenfunction expansion method, yielding a solution with the form:

$$\mathbf{X}(t) = \sum_{k=1}^{n} \phi_k \exp(\omega_k t) b_k = \mathbf{\Phi} \exp(\mathbf{\Omega t})\mathbf{b} \tag{2}$$

Where ϕ_k and ω_k are the eigenvectors and eigenvalues of the matrix $\mathcal{A}$, the coefficients b_k are the coordinates of the system's initial conditions, $\mathbf{x}(0)$, projected onto the eigenvector basis, and n represents the bound on dimensionality introduced by the discretization of the dynamical system into n spatial points. It is also possible to approximate the dynamics of the system by discretizing them over the time interval of interest, yielding $k = 1, 2, ...m$ 'snapshots' of the system, each separated by some Δt:

$$\mathbf{x}_{k+1} = \mathbf{A}\mathbf{x}_k \tag{3}$$

where

$$\mathbf{A} = \exp(\mathcal{A}\mathbf{\Delta t}) \tag{4}$$

A solution to the system that is expressed using terms obtained from the discretized matrix $\mathbf{A}$ is of similar form as that in Equation (2) and is as follows:

$$\mathbf{x}_{k+1} = \sum_{j=1}^{n} \phi_j \lambda_j^k b_j = \Phi \Lambda^k b \tag{5}$$

In the discretized solution, ϕ_j and λ_j are the eigenvectors and eigenvalues of $\mathbf{A}$ respectively, b_j still represents the system's initial conditions projected onto the eigenvector basis, and n is still the number of spatial points in the system. Specifically within the DMD framework, the eigenvectors in Φ are called 'DMD modes' and contain the coherent structures underlying the physics of the system, and the eigenvalues in Λ govern the dynamics of each corresponding mode.

The matrix that represents the discretized dynamics of the system, $\mathbf{A}$, is optimally constructed so that it best fits the trajectory of $\mathbf{x}$ between the k^{th} and k^{th+1} snapshots in the L2 sense,

$$||\mathbf{x}_{k+1} - \mathbf{A}\mathbf{x}_k||_2 \tag{6}$$

When considering the full range of snapshots $k = 1, 2, ..., m$, the matrix $\mathbf{A}$ that minimizes

(1.6), will change from snapshot to snapshot. Thus, to find a matrix $\mathbf{A}$ that will best linearly approximate the dynamics across *all* snapshots, a slightly different regression technique is employed. The data across all m snapshots is organized into two large matrices,

$$\mathbf{X} = \begin{bmatrix} | & | & ... & | \\ \mathbf{x}_1 & \mathbf{x}_2 & ... & \mathbf{x}_{m-1} \\ | & | & ... & | \end{bmatrix} \tag{7a}$$

$$\mathbf{X}' = \begin{bmatrix} | & | & ... & | \\ \mathbf{x}_2 & \mathbf{x}_3 & ... & \mathbf{x}_m \\ | & | & ... & | \end{bmatrix} \tag{7b}$$

where each of the m column vectors are all the spatial measurements taken from the system at a specific point in time. The linear approximation of the dynamics between the two matrices is defined as,

$$\mathbf{X}' \approx \mathbf{A}\mathbf{X} \tag{8}$$

Here, the matrix $\mathbf{A}$ is the unique matrix that minimizes the Frobenius norm,

$$||\mathbf{X}' - \mathbf{A}\mathbf{X}||_F \tag{9}$$

The matrix $\mathbf{A}$ that minimizes (9), is the best fit linear approximation of the dynamics of the complex system across all snapshots in the data set. Even if the system being examined exhibits nonlinear dynamics, $\mathbf{A}$ still provides a locally linear approximation of the dynamics from snapshot to snapshot. The main thrust of the DMD method is to efficiently determine the behavior of $\mathbf{A}$ for a given data set, which leads to decomposition of the data into a set of dynamic modes that provide insight into the spatiotemportal coherent structures present in the system, as well as their associated time dynamics. An important assumption when using DMD is that the individual snapshots $\mathbf{x}_k$ in the matrix $\mathbf{X}$ are high dimensional, making the matrices $\mathbf{X}$ and $\mathbf{X}'$ tall and skinny. This assumption is usually valid when using snapshots generated from a high-fidelity CFD simulation, where the number of spatial points n is typically $\mathcal{O}(10^6)$ and above,while the number of snapshots m is typically $\mathcal{O}(10^2)$ to $\mathcal{O}(10^3)$ at most. If $\mathbf{A}$ were to be directly computed from the matrices $\mathbf{X}$ and $\mathbf{X}'$ of this size, the number of elements in $\mathbf{A}$ would be $\mathcal{O}(10^{12})$ or higher. Thus, a direct computation of $\mathbf{A}$ is intractable when n is large. The DMD method takes advantage of the fact that $m << n$, which in turn means that the matrix $\mathbf{A}$ is at most rank $m-1$. A low rank subspace can be defined by a set of $m-1$ POD spatial modes, and within this subspace a low rank representation of $\mathbf{A}$ can be computed. This low rank representation, defined as $\tilde{\mathbf{A}}$, contains at most $(m-1)^2$ elements, but still accurately captures how the dynamics of the system evolve across snapshots. The low rank dynamics are then reprojected into the full dimensions spanned by the dataset. This full dimensional reprojection of $\tilde{\mathbf{A}}$ contains an accurate reconstruction of the leading, dominant eigenvalues and eigenvectors of the orginal $\mathbf{A}$ matrix. Therefore, the DMD method can accurately capture the behavior of the $\mathbf{A}$ matrix, without an explicit computation of $\mathbf{A}$.

The DMD method provides many strengths as an analysis tool, such as being equation free, relatively simple to implement, and allowing for insight into the key underlying physics of a problem. However, the method has multiple weaknesses as well. Since the DMD method is based on the Singular Value Decomposition (SVD), it has the same difficulty in capturing non-stationary (unsteady and does not fluctuate about a mean) behavior in a dataset that the SVD does. Data sets that exhibit rotational and/or translational invariance across snapshots can lead to an artificial inflation of the low rank characterisation of the systems dynamics, and data sets that exhibit transient on/off phenomena may not be accurately captured at all.

1.1.2 Combined Time Frequency Analysis

When analyzing a data set, it is often useful to determine its underlying frequency content to gain insight into the range of frequencies the signals in a given data set span, and what components of the overall signal are important. When the data set being considered is an aerodynamic flow-field, frequency analysis can give insight to the nature of flow features like shock boundary layer interactions, separation characteristics, and turbulence. A common method of computing the frequency content of a signal is to perform the Discrete Fourier Transform (DFT), which is a discretized method of computing the analytic Fourier Transform. The DFT algorithm takes a vector of data points from some time series input signal $\mathbf{f}$, and maps them onto the frequency domain coefficients in the vector $\hat{\mathbf{f}}$. This is accomplished by multiplying the input vector by a linear operator, which in this case is the complex-valued Vandermonde matrix $\mathbf{W}$. Once the data has been transformed into the frequency domain, excellent frequency information can be obtained about the signal by viewing the Power Spectral Density (PSD). The PSD indicates how much power the signal contains at each of its frequency components, so the frequencies that are most important to the original signal can be determined. When DMD is applied to a set of snapshots, it acts like a data-driven DFT since each calculated mode will have a corresponding frequency.

A main drawback of the DFT is that when the signal is transformed into the frequency domain, all time information about the signal is lost. This drawback also applies to DMD. The loss of temporal information means that the DFT is best designed to analyze signals that are periodic in time, because it does not matter when in time a specific frequency is occurring for a purely periodic signal. However, real-world signals are often not periodic, and contain evolving frequency content over time. This motivates the use of methods that allow for determining both what frequencies are occurring in a given signal, and when in time these frequencies occur.

One analysis method that gives combined time and frequency information of a signal is the Short-Time Fourier Transform (STFT), which is also known as a 'windowed' Fourier

Transform. The STFT algorithm takes the normal Fourier Transform, and multiplies it by some windowing function that moves through time, and computes the frequency content of windowed function using the DFT. The formal definition of the STFT is given as,

$$\mathcal{X}(\tau, \omega) = \int_{-\infty}^{\infty} x(t)\omega(t-\tau)e^{-j\omega t}dt \tag{10}$$

where the resulting signal of the STFT transform, $\mathcal{X}(\tau, \omega)$, is a function of both frequency and some time window. The results of the STFT are the frequency spectra of the signal within the various time segments that are created by windowing the signal. The results of the STFT can be viewed using a three dimensional plot called a spectrogram, which is analogous to the two dimensional PSD from DFT analysis. When viewing a spectrogram the x, y, and z axes are time, frequency, and amplitude respectively. In Fig 1, the time series of a notional signal is shown, and its subsequent notional PSD and spectrogram results are shown to compare how the STFT and DFT decompose the same signal.

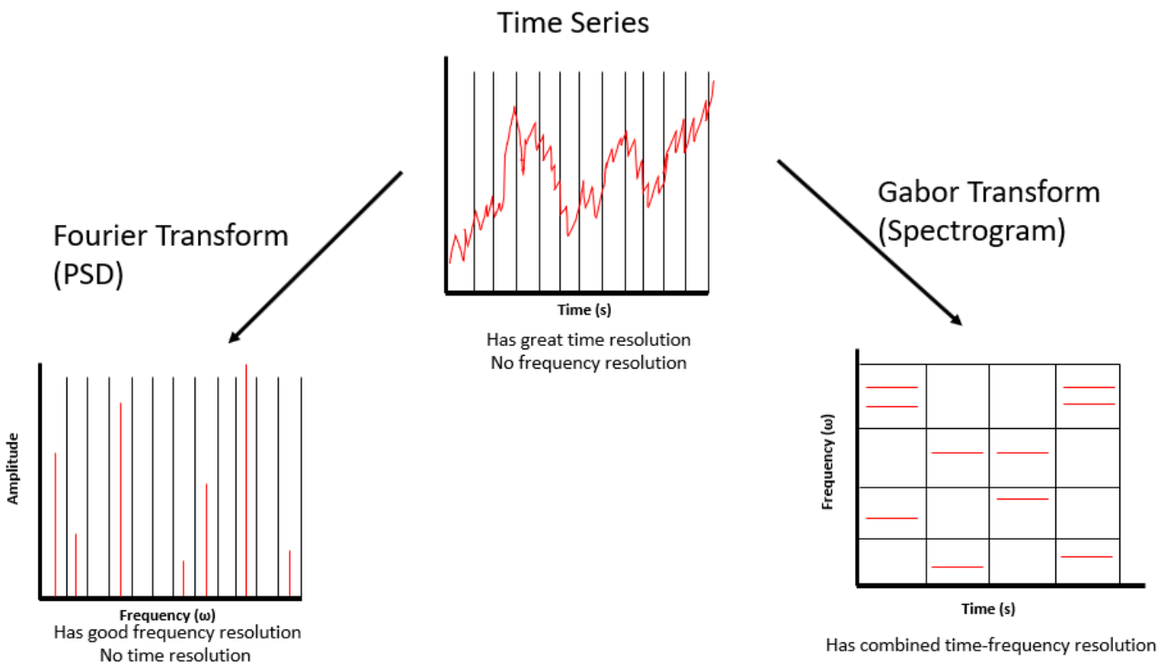

Figure 1: Notional time series of a signal and the results of its corresponding transformation via the DFT (left) and STFT (right)

The original time series plot of the signal has excellent time resolution, meaning that it is very easy to tell what the signal is doing at any given point in time. However, time series contains no frequency resolution, so it is impossible to tell what individual frequency components comprise the signal at any point in time. The results of the DFT contain excellent frequency resolution and no time resolution, since the entire signal was transformed from the time domain into the frequency domain. Consequentially, it is very easy to tell what frequencies make up the original signal, but there is no information that indicates when in time a given frequency is active in the original signal. As mentioned before this is not an

issue with purely periodic signals, since the same frequency information is repeated throughout time. For signals that contain non-periodic content that changes over time, obtaining information about what frequency components are occurring during a given time interval can give greater insight into the nature of the system. The results of the STFT do exactly this, capturing the signal's content with both some resolution in frequency and some resolution in time.

While the STFT combines some of the benefits of both time and frequency analysis, it retains information in poorer time and frequency resolution than pure time series or DFT analysis respectively. This result stems from the Uncertainty Principle of quantum mechanics, and its extension to signal processing. In the same way a particle can never be measured as a point in the position-momentum plane, a signal can never be measured as a point in the time-frequency plane [1]. The limit of this uncertainty is known as the Gabor Limit, and is mathematically expressed as,

$$\sigma_t \sigma_f \geq \frac{1}{4\pi} \tag{11}$$

where σ_t and σ_f are the standard deviation estimates of time and frequency respectively. Variation of the size of the windowing function used in combined time-frequency analysis, which in turn changes σ_t, can lead to different 'resolution schemes', like the ones depicted in Fig 2.

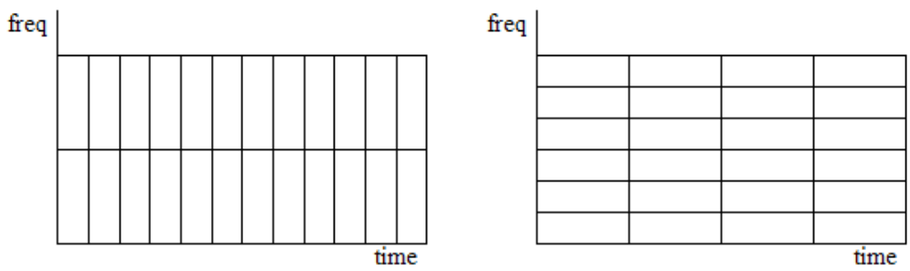

Figure 2: STFT analysis resolution scheme when using a short time window (left) and a long time window (right), from [1]

Shortening the time window leads to increased temporal resolution, but decreased frequency resolution, while lengthening the time window has the inverse effect. Changing the resolution scheme for a given signal can improve the results of combined-time frequency analysis, but the fixed nature of resolution scheme makes the STFT ill-suited for analysis of signals that exhibit multiple scales in both frequency and time. As is often the case with real-world systems, like unsteady, turbulent flow-fields, the time and spatial scales are broadband in nature and are difficult to analyze with fixed resolution schemes.

To extend the capabilities of combined time-frequency analysis to resolve a signal at varying time and frequency scales, multi-resolution analysis (MRA) and wavelets are often employed.

MRA takes advantage of the natural relationship between frequency and time to produce better time-frequency information about a signal. Lower frequency signals take longer in time to complete a given number of cycles, so the there is not as much need to be precise about when in time these lower frequency signals are active. The inverse concept applies to high frequency signals, since they can finish a given number of cycles in a much shorter time period. Using this natural time-frequency relationship, MRA performs a hierarchical time-frequency analysis that gives good frequency resolution but poor time resolution for the lowest frequency components of signal, and good time resolution but poor frequency resolution for the higher frequency components of a signal. An example of this time-frequency hierarchy is depicted in Fig 3.

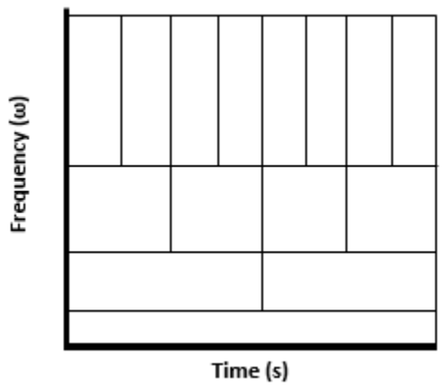

Figure 3: Example of multi-resolution analysis time-frequency hierarchy

Multi-resolution analysis still abides by the same uncertainty principle as stated in Equation (11), but the standard deviation terms are manipulated when looking at different frequencies ranges that comprise the original signal. When lower frequency bands are being analyzed, less temporal resolution is required, so the σ_t term can be increased. This in turn allows the σ_f term to be decreased, yielding improved frequency resolution. As higher and higher frequency components are analyzed, more temporal resolution is required to determine when in the evolving time-signal they occur. Following (11), this leads to poorer frequency resolution for higher frequency signal components. However, the multi-resolution scheme enables MRA to be better suited for analysis of realistic, time evolving signals.

As was done with the Discrete Fourier Transform mapping a time signal onto the frequency domain, and the Short Time Fourier Transform mapping the signal onto a fixed resolution time-frequency domain, some new transform must be applied to a time signal to map it onto the hierarchical time-frequency domain. This is accomplished with the Wavelet Transform. The Wavelet Transform takes a time signal, and projects it through function space into the wavelet domain where the basis functions are complex functions known as wavelets. This process is a generalized extension of how the Fourier Transform projects a signal through function space into the frequency domain, where the basis functions are sines and cosines

[10]. As is the case with the Fourier Transform, angles between vectors in the old and new domains are preserved since the new basis functions are mutually orthogonal.

Determining a set of basis functions for the Wavelet Transform begins with defining a general function known as the 'mother wavelet', and then scaling and translating the mother wavelet to create a family of basis functions:

$$\psi_{a,b}(t) = \frac{1}{\sqrt{a}}\psi\left(\frac{t-b}{a}\right) \tag{12}$$

Here, a and b are the mother wavelet's governing parameters, with a responsible for scaling the frequency band a wavelet can capture, b responsible for translating the time segment a wavelet captures. When a is equal to 1, and b is equal to 0, $\psi(t)$ represents the mother wavelet. The mother wavelet is some function that is constructed such that it is orthogonal to subsequent iterations of itself, when scaled according to Equation (12). Since the wavelet functions form an orthogonal basis and the basis functions can be scaled to cover different heights and time periods in the space they define, wavelets are ideal for projecting a time series signal into the multi-resolution time frequency domain. This is formally defined as the inner product of the time series vector f, and a family of wavelet basis functions $\psi_{a,b}$:

$$\mathcal{W}_\psi(f)(a,b) = \langle f, \psi_{a,b} \rangle \tag{13}$$

Wavelets and multi-resolution analysis were developed independently in the fields of mathematics, quantum mechanics, seismology, and electrical engineering. Modern developments in wavelet theory have led to their application in image compression, vision science, and turbulence analysis [11]. There are hundreds of types of wavelets, each tailored to a specific kind of analysis, but they are all able to be scaled and translated while retaining orthogonality which enables them to hierarchically extract time-frequency information from a signal. This hierarchical extraction not only allows for more precise analysis across different time and frequency scales, but also gives MRA the ability to extract on/off transients in a signal that might otherwise be missed by fixed resolution analyses. Both of these benefits make wavelets and MRA a very attractive option for analyzing the realistic, broadband, time evolving signals that arise from complex dynamical systems.

1.1.3 Multi-Resolution Dynamic Mode Decomposition

As mentioned previously DMD acts as a data driven Fourier Transform of the entire dynamical system being considered, with each mode acting as a frequency component of the original dynamics. Consequentially, DMD suffers from the same inability of the Fourier Transform to retain any temporal information about the system because the entire time series of snapshots taken from the dynamical system are considered. As a data-driven method, this makes DMD amenable to complex systems that are statistically stationary, i.e. systems that are unsteady but exhibit dynamics that oscillate around a mean position. However, systems of interest often display dynamics that will evolve over time, and contain underlying coherent structures

that span multiple frequency and time scales. Due to the large nature of data sets being generated with modern computational and experimental tools, the combined time-frequency analyses discussed in the previous section become difficult to apply to the entire system and extract meaning from the results. This motivates extending the data-driven nature of DMD to the hierarchical framework of multi-resolution analysis using the multi-resolution Dynamic Mode Decomposition (mrDMD) method.

To give mrDMD the ability to capture the underlying physics of a system, the same concept of hierarchical extraction of time-frequency information used in MRA is applied. It should be noted that mrDMD does not use wavelets like traditional MRA does, since the input to the algorithm is just the set of experimental or computational snapshots being considered. When applying the mrDMD algorithm to a set of snapshots, the user will define a number of levels of recursion, ℓ_{max}, that they want the algorithm to perform. At each level, the snapshots are divided into a number of time 'bins' (denoted as j), that each contain equal numbers of snapshots. The maximum number of bins per level is defined according to,

$$j_{max} = 2^{\ell - 1} \tag{14}$$

and each bin at each level contains $\frac{1}{j_{max}}$ of the snapshots. At each bin in every level, the DMD algorithm is applied to the proper set of snapshots. After each application of the DMD algorithm, some 'slow modes' are captured. These slow modes are the modes whose eigenvalues have the lowest magnitude in the complex plane, and consequentially represent the lowest frequency content in the data set. These slow modes are reconstructed into a time solution and then their influence is subtracted from the original set of snapshots. This is a data-driven approach to the hierarchical time-frequency analysis that wavelets perform. It should also be noted that the mrDMD algorithm divides the number of snapshots being considered in each bin by two as it moves up a level. A figure from [2] is shown to visually depict the recursive procedure of mrDMD.

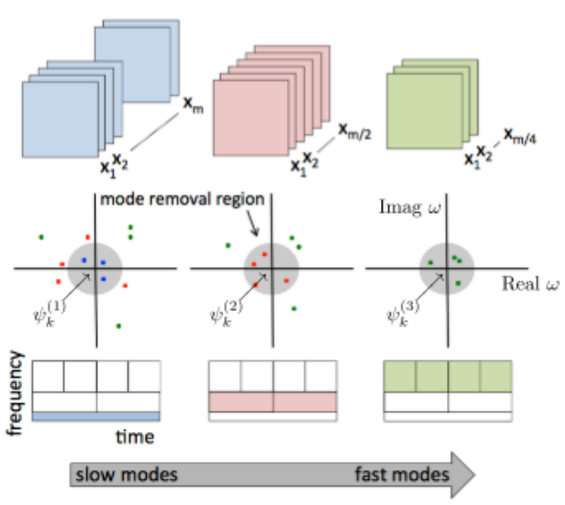

Figure 4: Visualization of mrDMD hierarchical analysis procedure, from [2]

The figure shows a notional 3 level mrDMD analysis. At the first level all m snapshots are considered. This is the same as performing a normal DMD algorithm on the snapshot set, but at the first level in mrDMD only the 'slow' DMD modes are retained. At the second level, $\frac{m}{2}$ snapshots are considered in each bin, and $\frac{m}{4}$ in each bin at the third level. The time-series reconstruction of the captured slow modes at each bin is calculated using Equation (5), and the influences of these slow modes on the original data set are removed using

$$\mathbf{X_{raw}}(\mathbf{t}) = \mathbf{X_{raw}}(\mathbf{t}) - \mathbf{X_{DMD_{slow}}}(\ell, \mathbf{j})(\mathbf{t}) \tag{15}$$

where $\mathbf{X_{raw}}(\mathbf{t})$ is the original full set of snapshots, and $\mathbf{X_{DMD_{slow}}}(\ell, \mathbf{j})(\mathbf{t})$ is the time reconstruction of the slow modes captured in the j^{th} bin at the ℓ^{th} level. As shown by (15), the original input data for the DMD algorithm can change for each new bin after slow mode reconstruction, since the influence of captured 'slow' frequency components are removed as the mrDMD algorithm completes its analysis. This component removal method follows the same hierarchical analysis procedure of wavelets and MRA, and is crucial for allowing transient patterns to be revealed by the data driven procedure.

For a DMD mode to be considered 'slow', the magnitude of its continuous time eigenvalue must fall below a certain threshold. This magnitude threshold is the radius of the grey circle denoted as 'mode removal region' in Fig 4. The radius for the region of removal, defined as ρ, is a user defined parameter in the mrDMD algorithm and there is relative freedom of choice in setting ρ based on the system being analyzed. Literature examples include setting ρ as a function of the number of cycles over the specific time-segment being considered [9]. In this work ρ is considered as both a Strouhal number threshold and a scalar that is inversely proportional to the time period of a given bin, to mimic the relationship in Equation (11).

mrDMD was developed to address the two main deficiencies of the base DMD algorithm, which are its difficulty to handle both data with on/off transients and data with translation/rotational invariance of low rank coherent structures. Using the same hierarchical framework of MRA, mrDMD can extract higher frequencies that are only active for a portion of the snapshots taken from the dynamical system. To try and overcome the deficiency of DMD at capturing non-stationary structures, mrDMD uses the idea that if a small enough time segment is considered a translating or rotating structure would appear stationary. Once the moving structure is close to stationary in a given time bin, mrDMD can accurately capture the structure and any associated dynamics. One drawback of mrDMD is that it is significantly more computationally expensive than the base DMD algorithm, due to its recursive nature. Certain techniques for improving the algorithm's efficiency exist, such as sub-sampling [2] and singular value thresholding [12]. The ability of mrDMD to overcome some of the deficiencies of normal DMD make it an attractive data-driven decomposition

method for problems that exhibit both highly transient and multi-scale physics.

1.2 Scramjets and Unstart

Vehicles that travel at hypersonic speeds ($M_\infty \gtrapprox 5$), have limited choice for propulsion systems. Rockets present one method for powering a craft at hypersonic speeds, but are not a desirable system for re-usable, sustained flight vehicles due to their relatively poor efficiencies and the weight penalty associated with carrying both fuel and oxidizer on board. Supersonic combustion ramjets, or scramjets, are an emerging alternative for hypersonic vehicles, since they are both more efficient than rocket engines and are air-breathing, eliminating the need to carry oxidizer as well as fuel. Due to the lack of traditional turbo-machinery in the flow-path of scramjets (and ramjets), sufficient compression and velocity reduction of the incoming freestream air must be achieved with a series of shock waves. The requirement for supersonic combustion in a scramjet compared to traditional subsonic combustion in a conventional ramjet stems from the losses associated with slowing supersonic flow to subsonic speeds. Decreasing high supersonic flow to subsonic speeds in the length scale of an engine inlet can lead to high stagnation pressure loses and separated internal flow, due to the strong shocks present in a super-sonic inlet [13]. Both of these consequences from inlet shocks reduce the efficacy of the compressive portion of the engine cycle, and subsequently overall thrust production. In order to abate these losses, scramjets slow the incoming high speed air to low super-sonic speeds, which lowers stagnation pressure loss and imposes a more favorable inlet pressure gradient. Due to their reduction of inlet/compression losses associated with slowing down incoming hypersonic flows to still super-sonic speeds, scramjets become the most efficient propulsion system, in terms of specific impulse (I_{sp}), starting around $M_\infty \approx 5$. A canonical plot of various propulsion systems, and their I_{sp} values versus freestream Mach number demonstrates the advantages scramjets possess in the hypersonic flight regime.

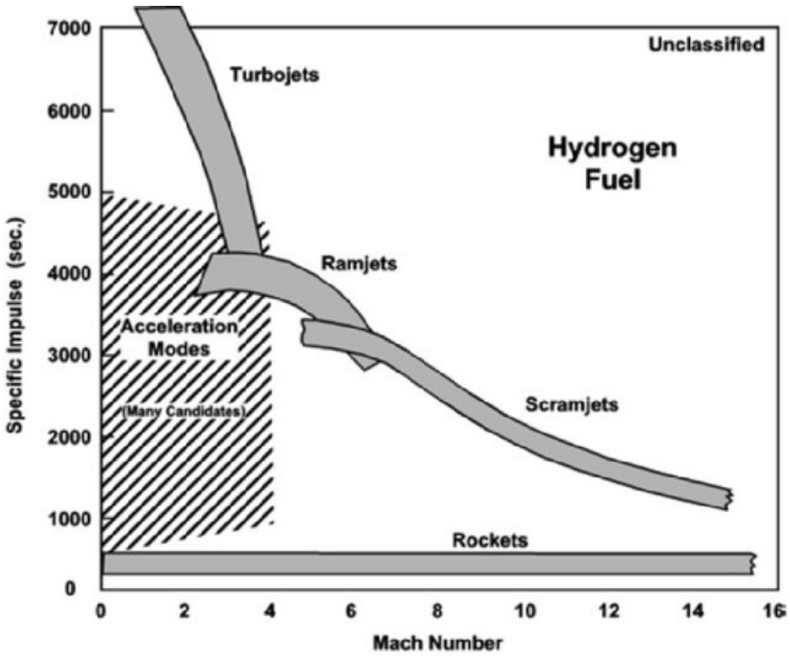

Figure 5: Canonical plot of various propulsion system I_{sp} versus M_∞, from [3]

The geometry of a scramjet is relatively simple, as outlined in Fig. 6a, due to its lack of moving parts. The main components of the engine are the inlet, the isolator, the combustion zone, and the nozzle. The inlet serves to first capture incoming hypersonic flow and direct it into the scramjet flowpath. Following the inlet, the flow enters the isolator portion. The isolator houses the series of shock waves used for compression and velocity reduction, also known as the Pre-Combustion Shock Train (PCST), as well as the area just downstream of the PCST where additional pressure changes due to mixing, heat addition, and area variation can occur [14]. This entire combined region of pressure rise is known as the 'pseudo-shock' and is outlined in Fig. 6b. The isolator is designed to contain this pseudo-shock and provide a buffer zone between the higher pressures of the combustion zone and the lower pressures of the inlet region of the flow-field. Following the isolator is the combustion zone, where supersonic combustion occurs. Combustion is often aided by flame-holder cavities, which promote fuel mixing and increase residence time [15]. The last portion of the scramjet is the nozzle, where the internal energy of the high-enthalpy flow is converted to kinetic energy via expansion to provide thrust.

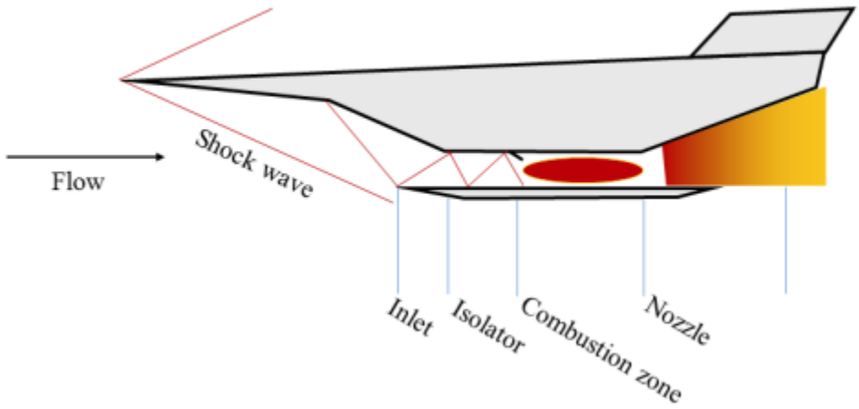

(a) Generic scramjet design, adapted from [16]

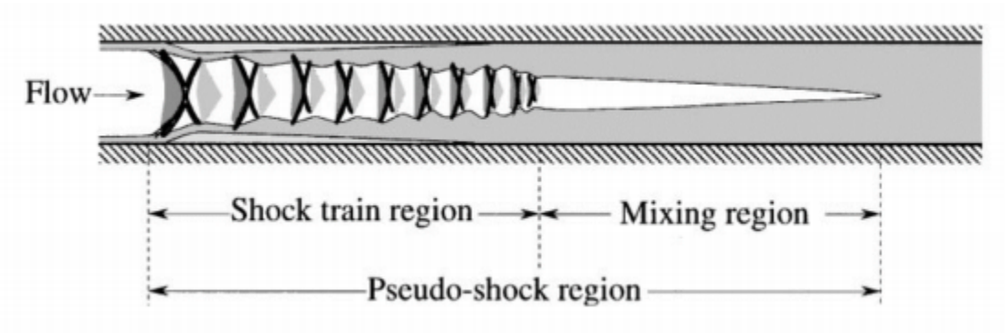

(b) Visualization of the pseudo-shock region held in the isolator portion of the scramjet, adapted from [16]

Figure 6: Overall scramjet design with pseudo-shock in isolator region highlighted

While the geometry of the engine is relatively simple, the harsh nature of the hypersonic flight regime introduces many complex physical phenomena that make the implementation of scramjet engines difficult. High temperature effects, non-equilibrium chemistry, and shock boundary layer interactions (SBLIs) combined with the short residence time of air within a scramjet present thermodynamic, structural, and gas-dynamic engineering challenges in each segment of the scramjet engine. One major challenge associated with the isolator portion of the scramjet engine is the phenomenon of unstart, where under certain conditions the PCST, which is critical to successful engine operation, is ejected upstream out of the inlet. The consequences of unstart are severe, with the engine ingesting a significantly reduced mass flow rate, which renders the engine unusable [17], and can even result in vehicle damage and loss [18].

The phenomenon of unstart is initiated by a pressure rise in the flow-field downstream of the isolator. In full scramjet systems, this pressure rise is often caused by an increase in heat-release associated with transient fuel-staging, as extensively discussed in [16],[19], and [20]. Experiments considering unstart often use mechanical flaps to mimic this pressure rise and simplify the flow-field, as outlined in [21]. If the pressure rise is large enough, boundary layer separation will occur within the isolator, and the pressure rise information

is freely propagated upstream through the subsonic, separated region of the flow-field. As the separation and pressure rise moves upstream, the supersonic core area of the flowpath is reduced [22], the shock train morphs into a more lambda-like structure, and the SBLIs vary in nature. When considering combustion induced unstart, thermal choking effects must also be considered in the rear portion of the isolator near the combustor entrance. While the isolator is designed to contain the pressure rise between the combustor and inlet, all the aforementioned flow-physics associated with combustion-induced heat-release or panel-induced back-pressure increase can create a pressure gradient across the isolator portion of the flow-field that will begin to drive the PCST forward and ultimately lead to full isolator/inlet unstart.

To maintain successful engine operation, the scramjet isolator must contain the pseudo-shock portion of the flow-field, and in doing so successfully provides a region where the pressure-rise associated with combustion does not directly distort the flow at the engine inlet. A longer isolator provides a longer region where this pressure rise can be modulated, but will cause adverse weight penalties and impractical length scales for its associated engine. Shorter isolators offer a weight advantage, but are more prone to unstarting due to their reduced length margins that can contain the PCST. A desirable design compromise is a shorter isolator with some control system that prevents unstart by regulating the internal flow-field of the scramjet in order to retain the PCST within the isolator. In order to attempt to control unstart, identification of the key incipient dynamics and the conditions that precede them must be achieved, and control systems must be activated in the small time window between the initiation of an unstart event and full PCST ejection, which is $\mathcal{O}(ms)$ [16]. Attempts have been made to implement unstart control systems using boundary-layer bleeding [22], active control of fuel staging [23], water-cooled flap actuation [18], and cavity resonance [24].

1.2.1 Application of Modal Decomposition

The complex nature of the unstart problem requires rich, precise measurements to accurately capture the underlying dynamics occurring in the scramjet flowpath, and as such high-fidelity simulations offer an attractive method to analyze unstart. In order to quantify the captured flow-physics, data-driven modal decomposition can be employed to extract meaning from the complex flow that would otherwise be intractable. Given the non-stationary nature of the unstart problem, and the multi-scale, transient nature of the associated physics, modal decomposition techniques that only consider the entire time-series of simulation snapshots will not be optimal tools for analyzing unstart simulations, possibly making multi-resolution methods better for analysis

In an attempt to better identify the underlying dynamics of unstart, mrDMD is applied

to a high-fidelity simulation of a cavity-controlled isolator, with Mach 2.24 incoming flow. A 4 level mrDMD analysis, with parameters outlined in Chapter 2, is performed to see if the hierarchical time-frequency analysis of mrDMD can better capture the meaningful dynamics of the unstart case. A normal DMD analysis is also performed, and the results are compared in Chapter 3. Due to the highly transient nature of the database being analyzed, results obtained from both the DMD and mrDMD analyses need to be interpreted with care. Modes may not have real physical significance, since the DMD algorithm is just approximating the underlying dynamics across all snapshots as outlined in (6), and characterizing non-stationary flow features such as PCST and separation region movement into pure frequency components. Additionally, both the number of snapshots taken from unstart database, and only a 4 level mrDMD analysis may not be sufficient for overcoming the translation/rotational invariance issues DMD experiences. However, the results of mrDMD and DMD are still be compared to each other, to demonstrate any benefits the former algorithm has over the latter for a non-stationary problem like scramjet unstart.

Chapter II: Methodology

2.1 Singular Value Decomposition

In DMD, as well as other decomposition techniques like POD, the Singular Value Decomposition (SVD) is the core mathematical technique used to extract low-rank patterns from high-dimensional data. The SVD is a well known, robust, numerically stable, and efficient method for data-driven matrix decomposition that is commonplace in engineering and scientific applications. Since SVD is the driving force of the DMD and mrDMD algorithms, it is worthwhile to briefly explore the SVD, and to also review its shortcomings when applied to non-stationary data.

The SVD is formally defined as

$$\mathbf{T} = \mathbf{U}\mathbf{\Sigma}\mathbf{V}^* \tag{16}$$

where $\mathbf{T}$, is a general n x m matrix, $\mathbf{U}$ is an n x m matrix copmrised of the left singular vectors, $\mathbf{\Sigma}$ is an m x m diagonal matrix containing the singular values, and $\mathbf{V}^*$ is an m x m matrix containing the right singular vectors. Matrices of these sizes allow for the most efficient computation of the SVD since only the first m non-zero singular values are considered, and as such this method is called the 'economy sized' SVD. It should be noted that the $\mathbf{U}$ and $\mathbf{V}$ matrices are both unitary and have orthonormal columns, and $\mathbf{\Sigma}$ only contains positive, real valued entries. The $\mathbf{U}$ and $\mathbf{V}$ matrices provide a column basis and row basis of the original $\mathbf{T}$ matrix, and can be thought of as storing the column and row patterns from the original matrix respectively. When regarding a time-series of snapshots, the left singular vectors can be thought of as containing the spatial patterns of the snapshot series, while the right singular vectors contain the temporal patterns.

The 'Achilles heel' of the SVD is that it can not efficiently handle matrices that exhibit translational/rotational invariance, or on/off transients [25]. To give an example, consider a matrix, $\mathbf{X}$, that contains m snapshots taken from a simulation of a travelling wave. The wave travels across all spatial points n, during the simulation but the number of spatial points the wave takes up is $<< n$ in a given snapshot. As the snapshots move from $1 \rightarrow m$, the set of spatial points the wave occupies in the column vector will vary greatly. The SVD will not view this as one, strongly correlated coherent spatial pattern moving through time, but will view it as many weakly correlated waves that occur at all points in time. A similar issue occurs with on/off transients, where the phenomena are poorly captured since they do not persist as a coherent pattern across all m snapshots. This exemplifies why SVD based methods are poorly equipped to handle non-stationary data, and motivates the use of methods such as mrDMD.

2.2 Dynamic Mode Decomposition

As previously stated, DMD decomposes a flow-field into a set of spatial modes and also computes the time dynamics associated with each mode. The dynamics of a given mode are represented as an oscillation frequency with a corresponding growth/decay rate. The most modern definition of DMD, as formulated by Tu et al, is outlined in this section according to the algorithm found in [9].

The goal of DMD is to linearly approximate the dynamics of a complex system across all m snapshots taken from the system, as outlined in Section 1.1.1. Restating 7a and 7b for convenience, the snapshots are first divided into two n x $m-1$ matrices,

$$\mathbf{X} = \begin{bmatrix} | & | & ... & | \\ \mathbf{x}_1 & \mathbf{x}_2 & ... & \mathbf{x}_{m-1} \\ | & | & ... & | \end{bmatrix} \tag{7a}$$

$$\mathbf{X}' = \begin{bmatrix} | & | & ... & | \\ \mathbf{x}_2 & \mathbf{x}_3 & ... & \mathbf{x}_m \\ | & | & ... & | \end{bmatrix} \tag{7b}$$

where n is the number of spatial points measured in the system, and m is the total number of snapshots. The two matrices contain all the time evolving measurements of the system, and the two matrices are separated by one time step. The dynamics of the system are approximated by the discrete linear operator $\mathbf{A}$, previously given as

$$\mathbf{X}' \approx \mathbf{A}\mathbf{X} \tag{8}$$

Since the $\mathbf{X}$ and $\mathbf{X}'$ are known, the unique $\mathbf{A}$ matrix that contains the local least squares approximation of the entire system's dynamics can be solved using the following relationship:

$$\mathbf{A} = \mathbf{X}'\mathbf{X}^{\dagger} \tag{18}$$

Here, $\mathbf{X}^{\dagger}$ denotes the Moore-Penrose pseudo-inverse, which is a generalized inverse for non-singular, rectangular matrices [26]. It is important to note that determining the nature of the dynamical matrix $\mathbf{A}$ via an eigendecomposition is the main thrust of the DMD method, as this matrix contains all relevant information on how the linear approximation of the system's dynamics will evolve. The eigenvectors of $\mathbf{A}$ are the dynamic modes, or DMD modes, of the system of interest, and each eigenvalue of $\mathbf{A}$ govern the dynamics of a corresponding mode. If $\mathbf{X}'$ and $\mathbf{X}^{\dagger}$ are low-dimensional, this problem can become relatively trivial, but in practice, especially when considering high-fidelity simulations of complex dynamical systems, these matrices are very high-dimensional. The number of spatial measurements n, and temporal measurements m for such simulations are typically $\mathcal{O}(10^6)$ and $\mathcal{O}(10^3)$ respectively. Snapshot matrices of this size yield dynamical matrices, $\mathbf{A}$, that have $\mathcal{O}(10^{12})$ elements and

require at least $\mathcal{O}(10^{14})$ operations to compute using the most efficient matrix multiplication algorithms [27]. Thus with high-dimensional data sets the direct computation of $\mathbf{A}$ becomes intractable, even with modern processing power.

In order to avoid direct computation of $\mathbf{A}$ and its eigendecomposition, the DMD algorithm finds a low rank representation of $\mathbf{A}$ that accurately captures its leading eigenvalues and eigenvectors. This low rank approximation is denoted as $\tilde{\mathbf{A}}$. To compute $\tilde{\mathbf{A}}$, the matrix $\mathbf{A}$ is projected into a low rank subspace provided by at most $m-1$ POD spatial modes. This procedure is outlined below.

First, the SVD of the first n x $m-1$ snapshot matrix $\mathbf{X}$ is taken, following the economy SVD approach,

$$\mathbf{X} = \mathbf{U}\mathbf{\Sigma}\mathbf{V}^* \tag{19}$$

The rank of the $\mathbf{U}$,$\mathbf{\Sigma}$, and $\mathbf{V}$ matrices can be reduced to some optimal rank r, as outlined in [12], but this further increase in rank reduction was not explored in this work. The pseudo-inverse of $\mathbf{X}$ is calculated using the SVD,

$$\mathbf{X}^\dagger = \mathbf{V}\mathbf{\Sigma}^{-\mathbf{1}}\mathbf{U}^* \tag{20}$$

Combining Equations 18 and 20 yields

$$\mathbf{A} = \mathbf{X}'\mathbf{V}\mathbf{\Sigma}^{-\mathbf{1}}\mathbf{U}^* \tag{21}$$

Here, $\mathbf{A}$ is partially decomposed, but still represented in its original high-dimensions. $\mathbf{A}$ can be projected onto the rank reduced, orthogonal basis $\mathbf{U}$ using

$$\tilde{\mathbf{A}} = \mathbf{U}^*\mathbf{A}\mathbf{U} \tag{22}$$

Combining 21, 22, and simplifying yields

$$\tilde{\mathbf{A}} = \mathbf{U}^*\mathbf{X}'\mathbf{V}\mathbf{\Sigma}^{-\mathbf{1}} \tag{23}$$

Here, it is seen that $\tilde{\mathbf{A}}$ is an $m-1$ x $m-1$ matrix that is efficiently calculated by a series of low-dimensional matrices. $\tilde{\mathbf{A}}$ also retains the dominant behavior of $\mathbf{A}$, since $\mathbf{A}$ was projected onto a hierarchical orthogonal basis, provided by the POD modes $\mathbf{U}$. Thus computing the eigendecomposition of $\tilde{\mathbf{A}}$ gives insight into the dominant dynamics of the orginal system approximated in Equation (8). The eigendecomposition is given as

$$\tilde{\mathbf{A}}\mathbf{W} = \mathbf{W}\mathbf{\Lambda} \tag{24}$$

where $\mathbf{W}$ is a matrix whose column vectors are the eigenvectors of $\tilde{\mathbf{A}}$, and $\mathbf{\Lambda}$ is a diagonal matrix containing the eigenvalues of $\tilde{\mathbf{A}}$. Even though the $\tilde{\mathbf{A}}$ matrix is low-dimensional, it contains the leading and dominant portion of the high-dimensional $\mathbf{A}$ matrix, and the eigenvectors and eigenvalues from Equation 24 can be used to reconstruct $\mathbf{A}$ in high-dimensional space,

$$\mathbf{\Phi} = \mathbf{X}'\mathbf{V}\mathbf{\Sigma}^{-\mathbf{1}}\mathbf{W} \tag{25}$$

where $\mathbf{\Phi}$ is a matrix of the exact eigenvectors of $\mathbf{A}$, having the same n x $m-1$ dimensions as the original, high-dimensional snapshot matrices. The column vectors of $\mathbf{\Phi}$ have the exact same 'shape' as the original snapshots, and can be reconstructed as 'eigen flow-fields', that contain coherent, spatial structures that dominate the dynamics of the system. The corresponding complex eigenvalue, λ_k, for each DMD mode governs how the mode evolves in time, with the real portion determining the exponential growth/decay rate of the mode, and the imaginary portion determining the sinusoidal oscillator frequency of the mode. The eigenvalues in $\mathbf{\Lambda}$ represent the discrete time dynamics, and to obtain continuous time dynamics a process akin to the inverse of Equation 4 is performed on the eigenvalues:

$$\omega_k = \frac{\ln(\lambda_k)}{2\pi\Delta t} \tag{26}$$

Here Δt is the time step between snapshots, and in the base DMD algortithm it is required to be constant, although alternative approaches considering non-uniform sampling have been considered [28]. Using the low rank approximations of the eigenvectors and eigenvalues, a time reconstruction of the original system can be performed using the method outlined in Equation 2,

$$\mathbf{X_{DMD}}(t) \approx \sum_{k=1}^{n} \phi_k \exp(\omega_k t) b_k = \mathbf{\Phi} \exp(\mathbf{\Omega t})\mathbf{b} \tag{27}$$

where $\mathbf{b}$ is a column vector containing the initial amplitudes of the modes, and is calculated by projecting the modes onto the first snapshot,

$$\mathbf{b} = \mathbf{\Phi}^{\dagger}\mathbf{x_1} \tag{28}$$

The outlined DMD algorithm provides a data-driven modal decomposition that takes advantage of a low rank subspace to linearly approximate the underlying dominant dynamics of a complex system. As mentioned in Chapter 1, DMD will act as a Discrete Fourier Transform of the entire system, and as such the algorithm is amenable to stationary (unsteady but fluctuates about a mean point) data sets, or purely periodic systems. The method outlined in the subsequent section details the modifications made to the base DMD algorithm to enable it for multi-resolution analysis, in an attempt to make the method more applicable to non-stationary data sets.

2.3 Multi-Resolution Dynamic Mode Decomposition

As outlined in 1.1.3, mrDMD performs a recursive DMD procedure that hierarchically extracts coherent structures and their associated dynamics, acting as a multi-resolution scheme for data-driven time frequency analysis. Two user defined parameters are outlined in the first step of the algorithm; a number of levels, ℓ_{max}, and a radius of removal, ρ. The number of levels indicates the levels of recursion, i.e. how many times mrDMD will divide the number of snapshots into j_{max} bins and perform the DMD algorithm within each bin. It should be noted that the maximum number of bins at a given level, j_{max}, is given by $2^{\ell-1}$, with ℓ being the current level of recursion. The radius of removal, ρ, denotes the radius of a circle

in the complex plane, and all *continuous time* DMD eigenvalues that fall within the radius of removal ($|\omega_k| \leq \rho$) for a given bin, j_k, are considered 'slow modes' whose influence will be removed.

The entire mrDMD algorithm is a function of the matrix containing the entire time series of snapshots $\mathbf{X_{raw}}$, as well as the two user defined parameters ℓ and ρ. There is freedom of choice by the user in determining the two defined parameters. Since the number of time bins per level is determined by ℓ, this parameter is set based on the required time resolution of the analysis. The limiting factor with ℓ_{max} is the number of snapshots being considered. Since the snapshots considered per bin is halved at each level of recursion, a threshold where not enough snapshots to accurately capture the underlying physics can be reached quickly if m is small.

The radius ρ is set in a principled way according to the physics of the system in question. Two general formulas for determining ρ are considered in this work,

$$\rho = a\ell \tag{29a}$$

$$\rho = \frac{b}{T} \tag{29b}$$

where a and b are scalars, and T is the time period in seconds being considered by a given bin. 29a is used in this work in the validation step of the algorithm, where a is the Strouhal number ($a = St = 0.3$) of the lowest frequency SBLI's outlined in [29]. This was done to capture the dominant shock motion of the system at the first level of analysis, and higher frequency turbulent effects at higher levels. 29b defines ρ as the maximum number of cycles, b, that a frequency can undergo and still be considered 'slow' for a given bin. b can also be treated as a general scalar, used to mimic the relationship in Equation 11. This latter method is used in the application of the algorithm to the non-stationary case of unstart, where $\rho = \frac{7.96}{T}$, to generally capture higher frequency events as well as isolate shock train motion.

The mrDMD algorithm performs the DMD algorithm outlined in section 2.2 in each time bin at a given level. A time reconstruction of the slow modes captured in each bin is created as defined by the base DMD algorithm, and the full system can be represented by combining the reconstructions of all slow modes captured throughout the procedure. This is formally given as

$$\mathbf{X_{mrDMD}}(t) \approx \sum_{\ell=1}^{\ell_{max}} \sum_{j=1}^{j_{max}} \sum_{k=1}^{n} f^{\ell,j}(t) b_k^{\ell,j} \phi_k^{\ell,j} \exp(\omega_k t) \tag{30}$$

This expression can also be interpreted as finding the least squares fit of the dynamics of the system at each level and bin. It should also be noted the function $f^{\ell,j}(t)$ is a sifting function that zeros all data outside the current set of snapshots being considered. This can lead to artificially high frequencies near cut-off points, and other sifting functions such as wavelets have been proposed by Kutz et al [9].

Chapter 3: Results

3.1 Validation of mrDMD on Statistically Stationary Flow

Since little literature exists on applying mrDMD to complex, turbulent flow-fields the mrDMD algorithm created for this work was validated on the statistically stationary case of supersonic flow past a wall-mounted turret. The same database that was used for DMD analysis in [29], was used for validation. The dominant flow-physics for this database are unsteady SBLIs with a low Strouhal number ($St \approx 0.3$), the incoming turbulent boundary-layer, the separation zones both before and after the mounted turret, and the shear layer. The three latter coherent structures exhibit broadband frequency scales, since they are closed tied to the turbulence in the flow-field. A 5-level mrDMD analysis was applied to a series of 2000 snapshots of the density field from the database. Using the *a priori* knowledge of the underlying physics, the radius of removal was set as $\rho = 0.3 * \ell$, so that all dominant SBLIs were expected to be captured as 'slow modes' in the first level of the analysis. At higher levels of the mrDMD analysis, it was expected for the turbulent flow features to be identified, with the captured coherent structures becoming finer and finer in scale. It was also expected for the mrDMD results to match the DMD results from [29], since the system is statistically stationary and contains the same relevant frequency content at all points in time.

Successful implementation of the radius ρ as a function of the SBLI Strouhal number allowed the mrDMD algorithm to extract the mean density field and a dominant shock mode in the first level of analysis. The mean mode in Fig 7 and the shock mode in Fig 8 match the DMD results from [29], both in mode shape and in the dynamics associated with the eigenvalue of each mode.

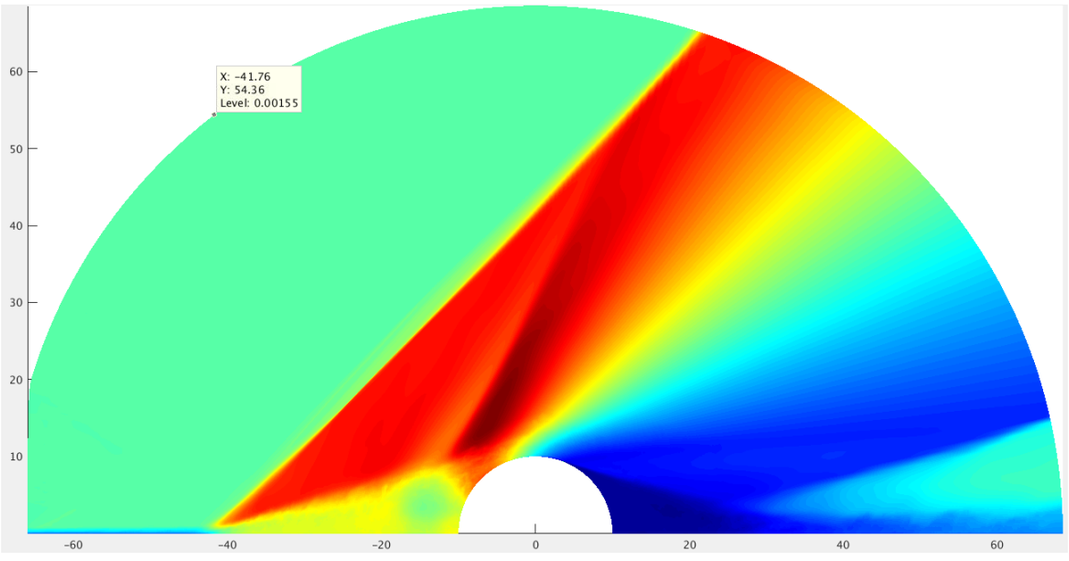

Figure 7: Density mean mode extracted from level 1 of mrDMD analysis

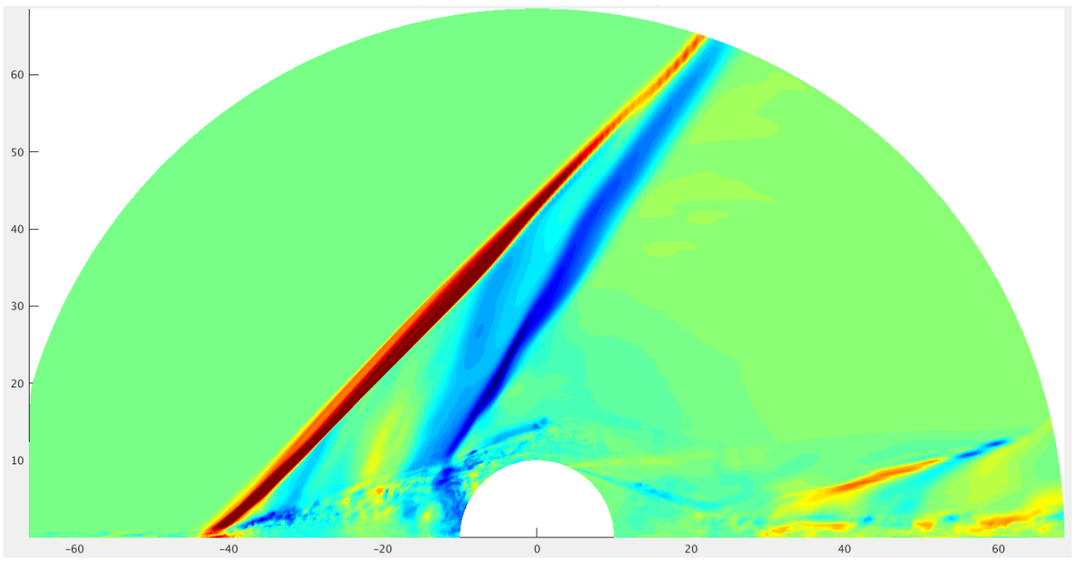

Figure 8: Shock mode extracted from level 1 of mrDMD analysis

At the third level of the mrDMD analysis, the turbulent boundary layer, separation regions, and reattachment zone become the dominant coherent structures that are captured. Some traces of the leading shock waves are still present at level three. At the fifth level of the analysis, the turbulent phenomena continue to dominate the dynamics, and the captured coherent structures are of finer scale with higher associated frequencies, as was expected. It should be noted that the described dynamics persisted through all time bins at levels 3 and 5 respectively, and the sample modes shown from these levels are representative of the general mode types present across all time bins at their respective level.

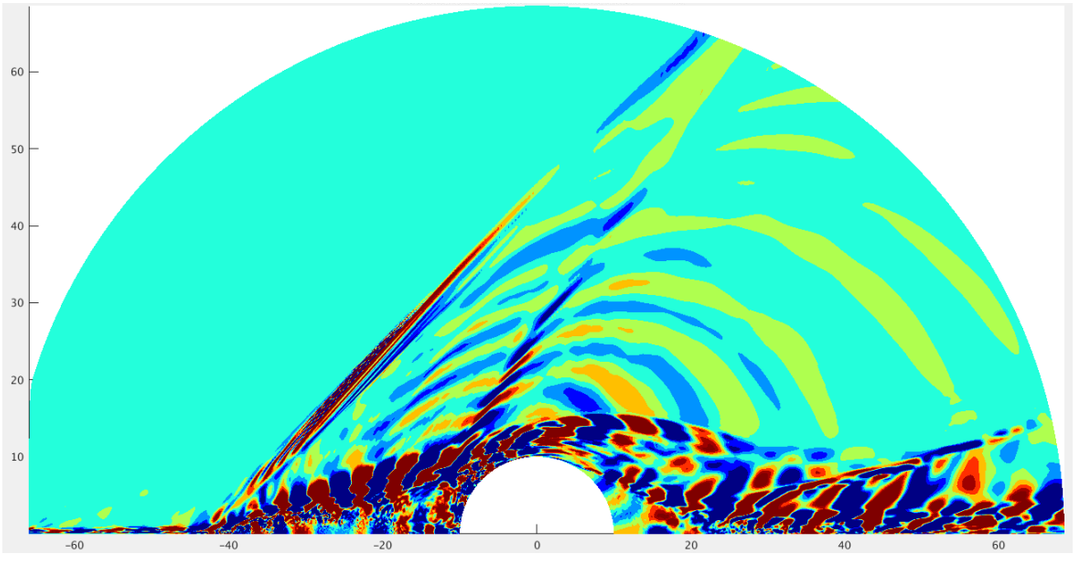

Figure 9: Mode with coherent structures of turbulent phenomena extracted from level 3, bin 1 of mrDMD analysis

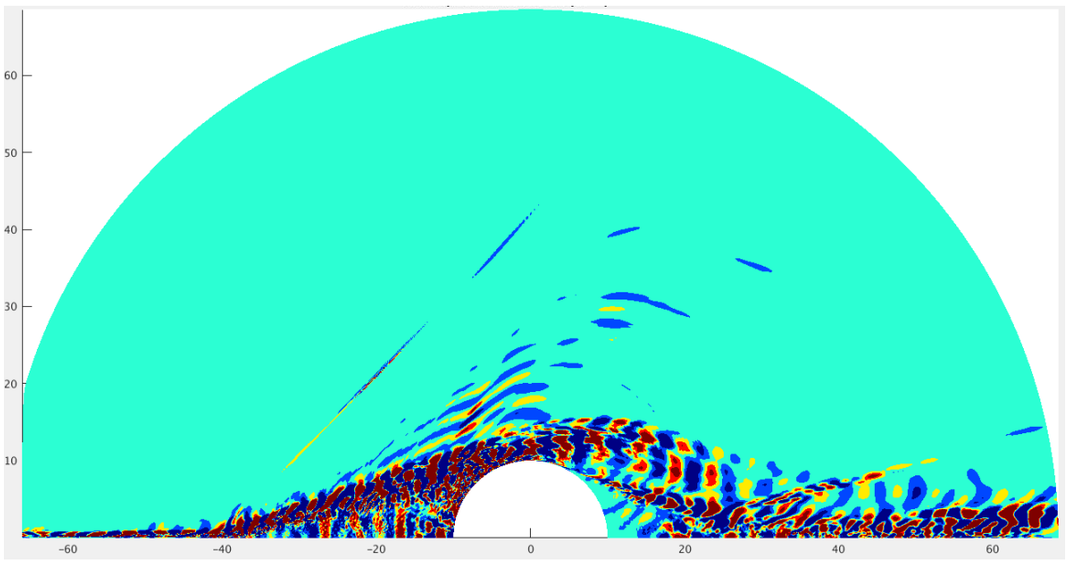

Figure 10: Mode with coherent structures of turbulent phenomena mode extracted from level 5, bin 10 of mrDMD analysis

The modes captured by the mrDMD algorithm matched the mode shapes from the DMD analysis in [29], and the frequency content from the new mrDMD analysis matched previous DMD results. For statistically stationary systems with no outlying events, normal DMD should be the variant of the algorithm used, since applying mrDMD is not as efficient as using the base DMD algorithm and yields the same results. In this case mrDMD was used to validate the newly developed algorithm and also show that the ρ parameter can successfully be set as a Strouhal number filter for oscillatory systems, assuming that a consistent non-dimensional time step is used to calculate the continuous time eigenvalues.

3.2 Description of Unstart Database

A LES of a scramjet isolator undergoing unstart was performed by Alspach in 2018 [24]. Flow enters the isolator with a Mach number (M_e) of 2.24, Reynolds number (Re) of 253,000, and a boundary layer thickness (δ) of 5 mm. In the simulation. unstart is induced by the pressure rise caused by a 31° ramp at the rear of isolator. The computational domain includes an upstream cavity with and L/D ratio of 3. Despite the high Re and complex flowpath, the simulation was performed in such a way that eddies were not resolved, and as such the internal isolator flow is laminar. For this work, only the 2-D slice taken through the flow-field center-z plane is considered. 489 snapshots of the u-velocity component were extracted for use in the DMD and mrDMD algorithms, with each snapshot being separated by $\Delta t = 0.1s$.

3.3 DMD Results

The DMD algorithm calculated 488 dynamical modes that best locally and linearly represent the dynamics from the simulation snapshots. The full spectrum of the continuous time eigenvalues that correspond to these modes is shown in Fig 11. The dynamics associated with these calculated eigenvalues exhibit a range oscillatory behavior, with the frequencies

ranging from 0 to 5 Hz. 5 of the dynamical modes also exhibit a significant decay rate.

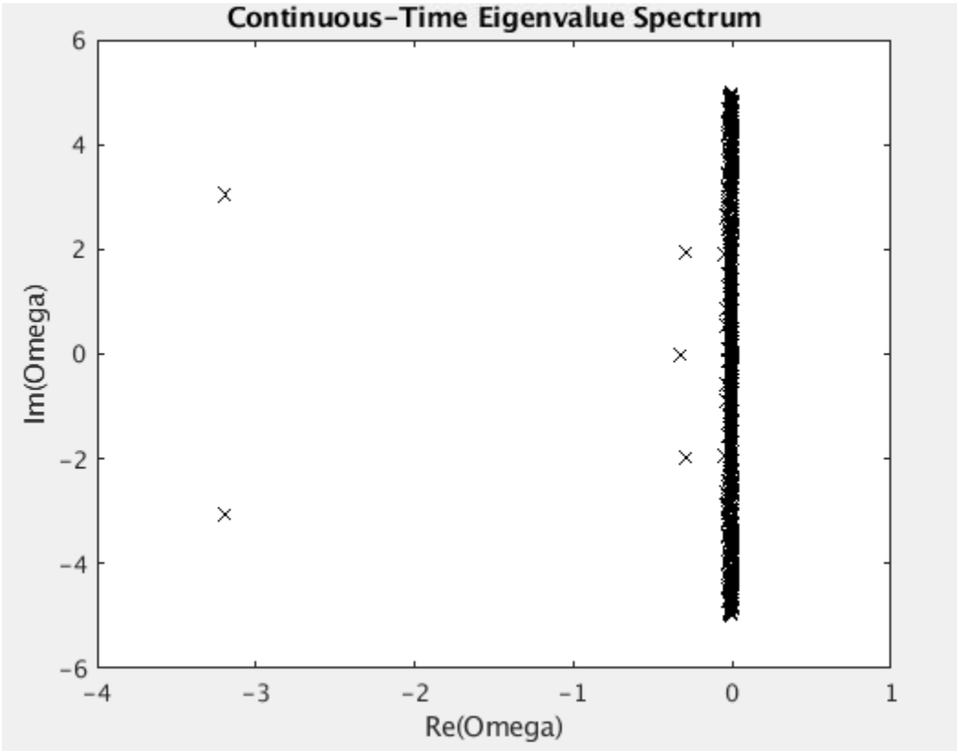

Figure 11: Continuous-time eigenvalue spectrum for DMD analysis of unstart simulation

The initial mode amplitudes, normalized by the maximum value in the **b** vector, are plotted with their associated frequency as well.

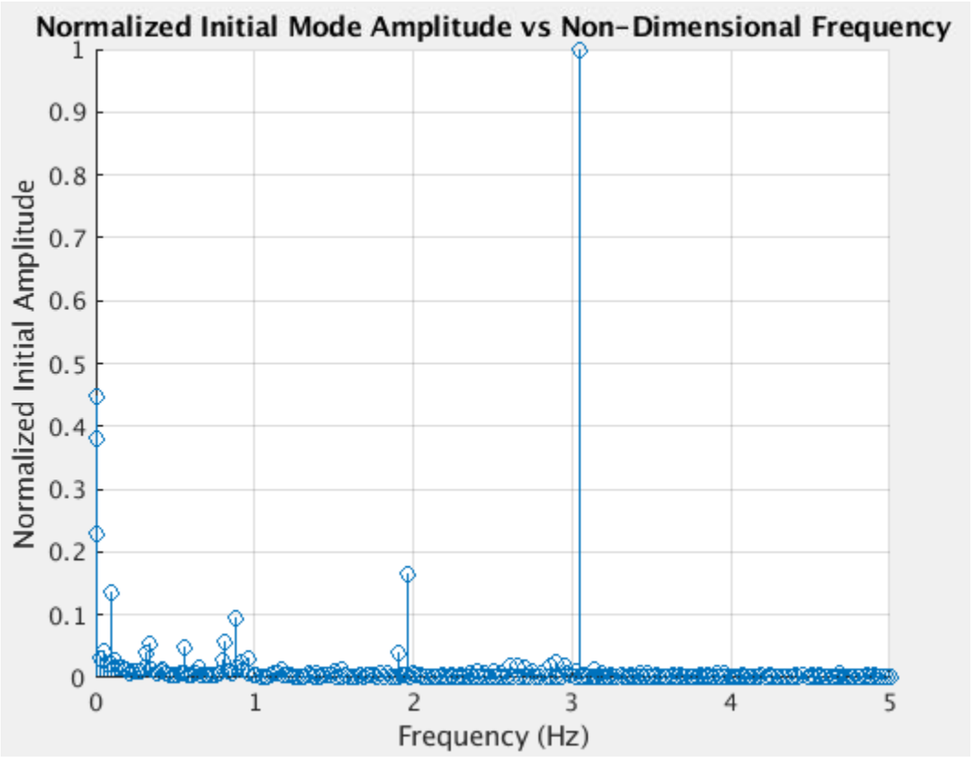

Figure 12: Initial mode amplitudes and frequency spectrum from DMD of unstart simulation

While the information in Fig 11 and 12 can provide meaningful insight for statistically stationary systems, for non-stationary systems the results might not correspond to anything

with physical meaning. In Fig 11, the frequency components of the system given by the DMD algorithm might only be the eigenvalues of the best fit linear operator **A**, without corresponding to the actual oscillatory behavior of coherent structures in the flow-field. A similar caution must be given for the initial mode amplitudes (**b**) in Fig 12, where how much a given mode is present in the first snapshot of the unstart simulation may have no real impact on the dynamical significance of a mode, since the flow-field evolves significantly over time.

Due to the time-evolving nature of the unstart flow-field, some of the DMD modes themselves might not have any physical meaning as well. However, some DMD modes were able to capture relevant coherent structures that are clearly present within the isolator flow-field during unstart. The mean modes that were captured by DMD contained signatures of the dominant separation bubble on the bottom isolator wall, some top wall separation, traces of the shock train, and also exhibited some shear layer dynamics associated with the cavity.

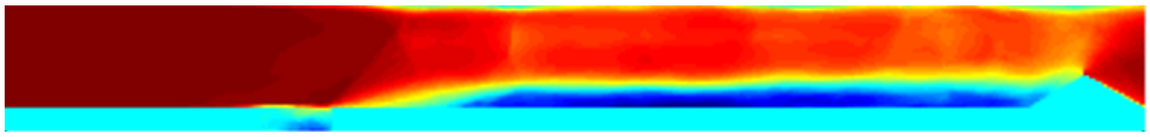

(a) First mean mode, shows large separation and some shock structures

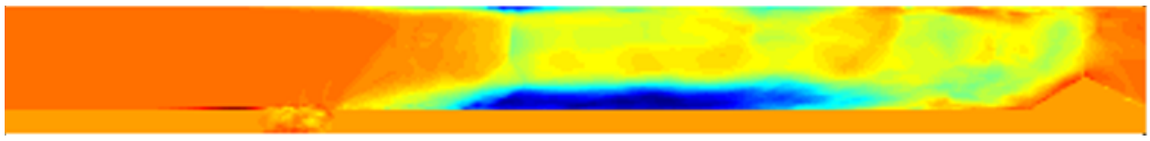

(b) Second mean mode, shows separation and some shock train signatures

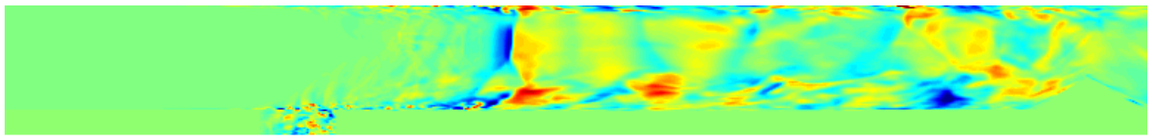

(c) Third mean mode, shows some PCST shock signature and cavity dynamics

Figure 13: Modes with $Im(w) = 0$ captured from DMD analysis (a) Mode 1/488 (b) Mode 2/488 (c) Mode 175/488

These mean modes exhibit some coherent structures that are present in the isolator during unstart, but these modes might not have physical significance since the flow-field evolves considerably over time, and time average would not accurately represent the flow-field. Some other modes of potential interest are the modes that exhibit a significant decay rate, shown by the five outliers in Fig 11. Of these five modes, one is the mean mode shown in Fig 13, and the other four are two sets of complex conjugates. All three of these mode sets exhibit a shock signature near the shear layer that extends from the cavity, as well as internal cavity dynamics.

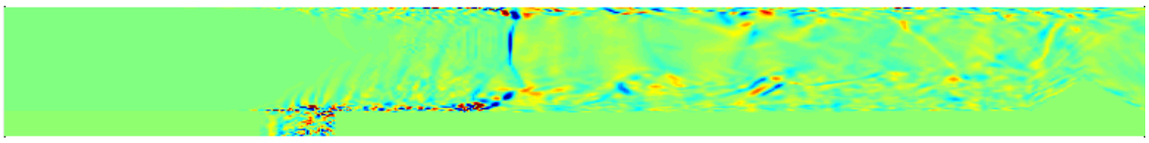

(a) Second decay mode, shows some shock structure, cavity dynamics, and cavity shear layer

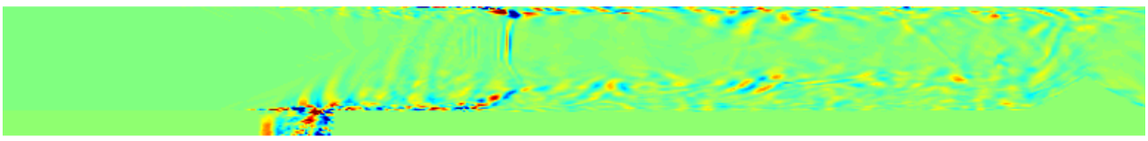

(b) Third decay mode, shows some shock structure, cavity dynamics, and cavity shear layer

Figure 14: Modes with significant decay rate captured from DMD analysis (a) Mode 483/488 (b) Mode 487/488

The modes in Fig. 15 could be representative of shock oscillation or shear layer frequency components in the unstart flow-field that are dynamically significant but decay quickly. The dynamical influence of these modes on the system could also not be physically significant due to the non-stationary nature of the data.

Another group of DMD modes of interest are those with the lowest magnitude eigenvalues. These could be representative of the dynamics in unstart with the lowest frequency content, which would likely be present for a longer time period during the unstart event. It should also be noted that these low magnitude eigenvalues were captured as slow modes in the first level of the following mrDMD analysis.

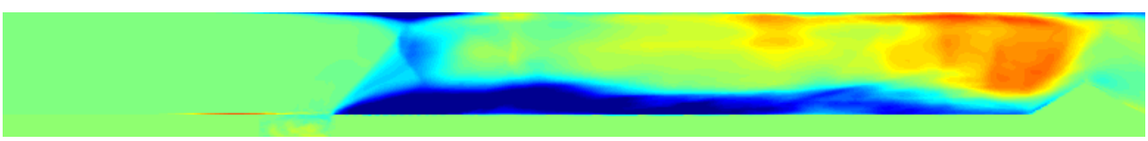

(a) Mode 4, shows separation and one dominant shock signature

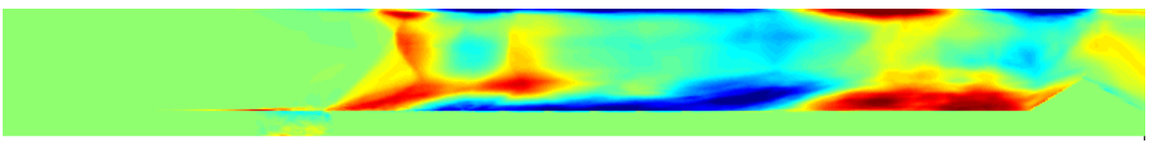

(b) Mode 6, shows less separation but contains multiple shock wave and shock cell signatures

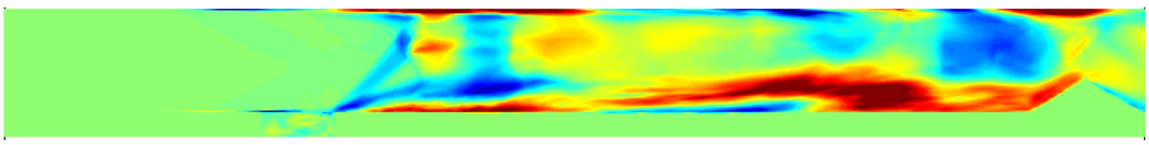

(c) Mode 8, shows shock train signature near cavity lip

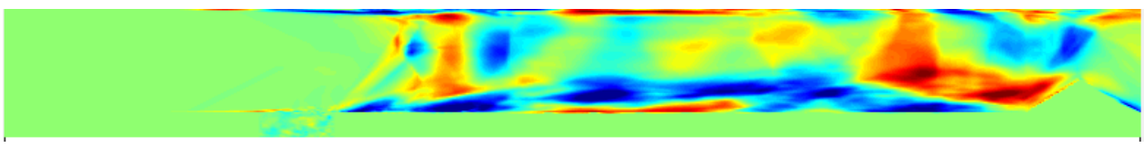

(d) Mode 10, shows compact shock train near cavity, as well as possible downstream shock behavior

Figure 15: Modes with low magnitude eigenvalues captured from DMD analysis, all with $|\omega_k| < 0.1$

These low magnitude eigenvalues generally capture some of the dominant coherent structures associated with the cavity-modulated isolator unstart case, such as large separation regions, cavity shear layer deflection, shock train signatures near the cavity lip, and some downstream shock activity, but in general do not show an indication of the upstream shock train and separation bubble movement that dominate unstart. This is likely due to the base DMD algorithm's inability to accurately capture coherent structures that exhibit statistically non-stationary behavior.

Some modes from the DMD analysis exhibited the signatures of many shocks, closely placed one after the other, as outlined in the red box in Fig 16

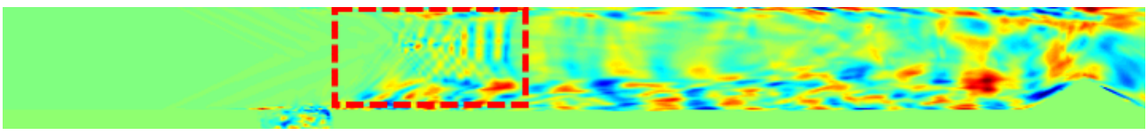

Figure 16: Mode 71/488, that exhibits a near cavity shock pattern that is closely stacked in the streamwise direction

This shock signature could be indicative of the issues SVD based methods have with objects that exhibit translational invariance across snapshots, like travelling waves. The SVD decomposition of the snapshots with travelling shock waves could be producing a basis of artificially high dimension, that treats the shock wave at each location as many independent coherent structures, rather than one structure moving through both space and time. This phenomena occurs with the SVD of a pure travelling wave, and leads to a POD basis with the wave at many distinct spatial points, which in turn creates a projection basis with not much physical meaning. This issue with representing a simple travelling wave in a data-driven way could be extending itself to the complex flow-field of the isolator undergoing unstart, where the moving, coherent shock wave structures are represented by a set of physically meaningless modes calculated with poor bases and singular values. This shock-trace feature was present in many of the modes, ranging from around mode 30 to mode 180. Two more sample modes that exhibit the stacking pattern are shown in Fig 17.

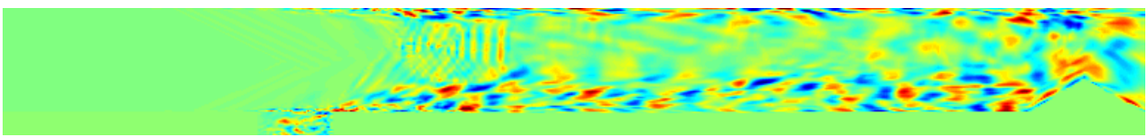

(a) Mode 113 that also exhibits shock-stacking pattern

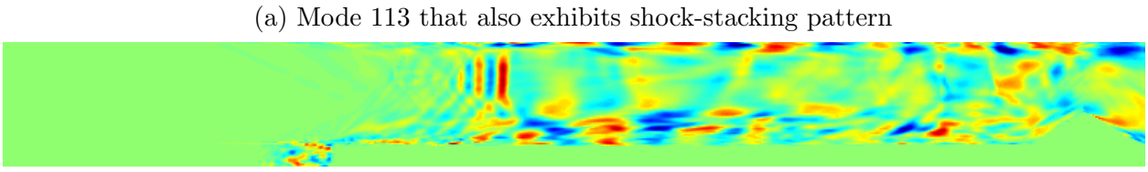

(b) Mode 177 that also exhibits the shock-stacking pattern

Figure 17: Sample modes that exhibit shock-stacking near rear lip of cavity

Many of the remaining modes, ranging from mode number 181 to 488, showed signatures of cavity dynamics, shear layer oscillation, and some intermittent flow behavior on the top and bottom walls of the isolator. These modes all had higher frequencies associated with their dynamics, with imaginary portions of their eigenvalues ranging from 1.86 to 5. Two sample modes from this range are given to provide an indication of what coherent structures the higher mode numbers captured.

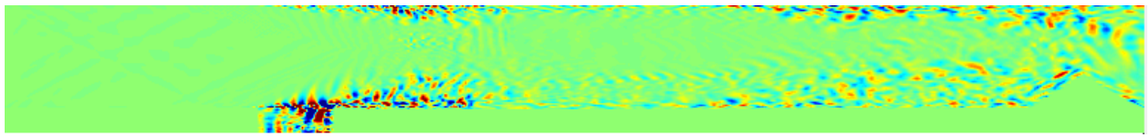

(a) Mode 229 that exhibits some shear layer deflection

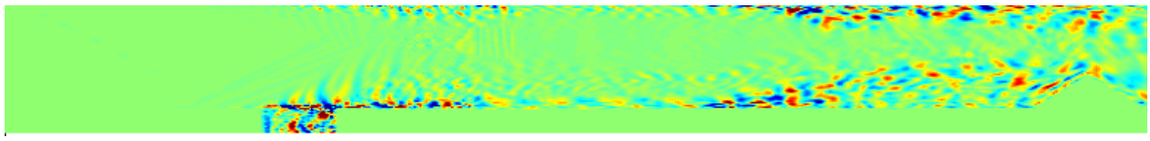

(b) Mode 324 that exhibits cavity dynamics and some intermittent downstream wall activity

Figure 18: Sample modes from the higher frequency range

All of the general mode shapes of interest captured by the DMD analysis exhibited some coherent structures that are present in the unstart simulation, such as shock structures near the rear lip of the cavity, large bottom wall separation, shear layer oscillations and deflection, and internal cavity dynamics. The DMD modes failed to capture the forward movement of the PCST from the rear portion of the isolator, the growth of the bottom separation bubble, and the development of shock/cavity interactions, all of which are dynamically important events that need to be identified and modeled for control systems to be accurately developed. Additionally, the DMD modes possibly exhibited evidence of the SVD failing to characterize spatio-temporal patterns in the data associated with shock movements, which reinforces that DMD is a poor tool for data-driven modeling of scramjet unstart.

3.4 mrDMD Results

A four-level mrDMD analysis was performed on the unstart database. The radius of removal parameter was set as $\rho = \frac{7.96}{T}$, where T is the time period being considered in each specific time bin (j_k). The ρ parameter was set in this manner to capture > 10 slow modes at level one. This was determined by plotting the full continuous time eigenvalue spectrum from the DMD analysis, and setting a radius that would capture the desired number of modes. The ρ parameter is also set as $f(\frac{1}{T})$ to mimic the time-frequency resolution trade-off in MRA. The mrDMD modes from level one are not presented in this section, as they are identical to the low magnitude eigenvalue modes from Fig 15. Although not all first level mrDMD modes are presented in Fig 15, the general 'shape' of those not depicted is the same. To identify any benefit mrDMD has over DMD at identifying the underlying dynamics in the time-evolving isolator flow-field, sample mrDMD modes from levels 2 and 3 are compared to DMD modes and instantaneous u-velocity snapshots. Sample mrDMD modes from level 4 are presented

on their own, to show how the dynamics of the non-stationary database are captured at the highest level of algorithm recursion. It should also be noted that a given level and bin are referred to as (ℓ_i, j_k).

3.4.1 mrDMD Level 2

At the second level of the analysis, the time series of snapshots is divided into two time bins, each containing 244 instantaneous u-velocity field measurements. In the first half of the snapshots, the PCST resides in the rear portion of the isolator and slowly moves upstream. In the second half of the snapshots, the PCST reaches the rear lip of the cavity and a large region of separated flow develops along the bottom wall. An instantaneous snapshot from each half of the time-series is depicted in Fig 19, as well as a DMD mode that best depicts the dynamics of the flow-field, and a mrDMD mode from both $(2, 1)$ and $(2, 2)$.

(a) Snapshot 220/489, shows PCST in back half of the isolator

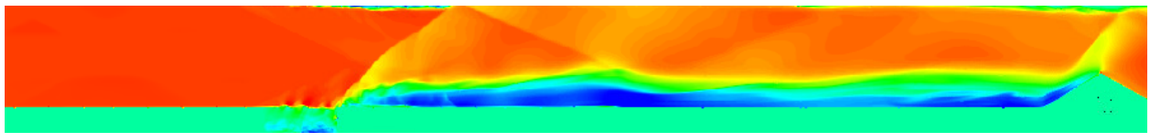

(b) Snapshot 350/489, shows shock train and separation bubble at cavity rear lip

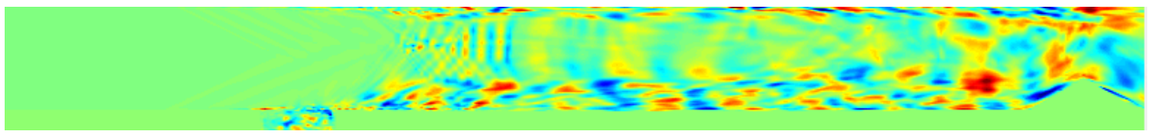

(c) DMD mode 71, shows shock signature near cavity and some downstream activity

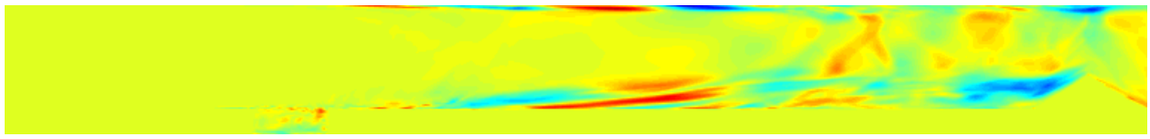

(d) mrDMD(2,1) mode 4, identifies shock train in rear section of isolator

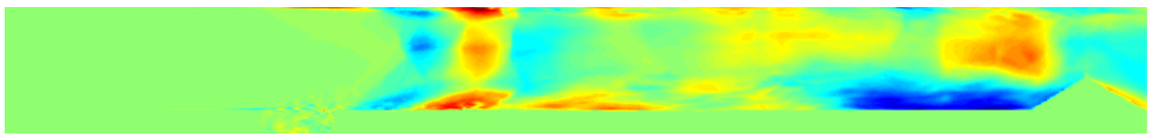

(e) mrDMD(2,2) mode 8, shows shock trace near cavity

Figure 19: Snapshot, DMD mode, and mrDMD mode comparison for level 2

mrDMD was able to identify the shock train in distinct locations at the second level of analysis, which is indicative of mrDMD being able to identify relevant coherent structures as they move throughout the flow-field over time. Shock-train movement and separation bubble growth are indicated in the mrDMD modes from (2,1) and (2,2), which was not discernible in the higher DMD modes. Some lower DMD modes better capture the coherent structures of the flow-field than mode 71 used for comparison in 19, but these modes all have low magnitude eigenvalues and were captured as slow modes in the first level of mrDMD

analysis. This allows mrDMD to identify the movement of coherent structures with finer temporal resolution in addition to retaining the original DMD modes that best capture the underlying dynamics. It should also be noted that the data is highly non-stationary in the two smaller time bins at level two of the analysis, so the same caution when observing DMD modes must be applied to extracting dynamical information from the mrDMD modes.

3.4.2 mrDMD Level 3

At level three of the analysis shock train movement and shape, cavity activity, and separation development are much more clearly resolved in the captured modes than the modes in level two of mrDMD. Across the four time bins, the shock train clearly moves upstream, and the captured mrDMD modes accurately retain similar shock train geometry to what is observed in the instantaneous snapshots.

In the first time bin, the shock train is identified in the rear portion of the isolator near the ramp, and its physical structure is represented much more accurately than it is in any of the normal DMD modes. The slow modes in mrDMD(3,1) also indicate the development of top and bottom wall separation near the front of the shock train.

(a) Snapshot 95/489, shows PCST near the unstart inducing ramp

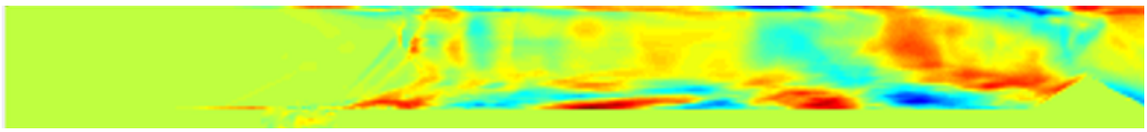

(b) DMD mode 20, that best captures shocks near ramp

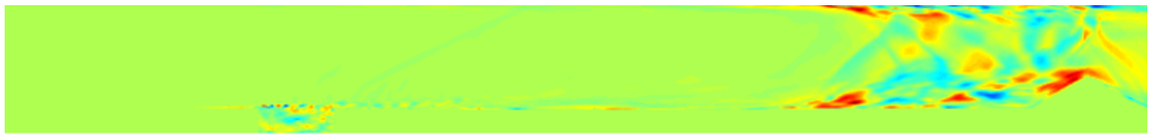

(c) mrDMD(3,1) mode 1, shows shock train near ramp

(d) mrDMD(3,1) mode 1, shows shock train and separation near front of shocks

Figure 20: Snapshot, DMD mode, and mrDMD mode comparison for level 3 bin 1

In the first time bin, mrDMD is able to resolve coherent structures of the flow-field that DMD completely fails to identify. The dynamics associated with these structures might still be physically insignificant, but the identification of coherent structures at their proper spatio-temporal location indicates mrDMD is much better at handling the non-stationary flow-field than DMD is.

In the second time bin, mrDMD is able to identify the shock train after it has moved slightly upstream due to the unstart-inducing pressure rise. In addition to identifying the shock train in a new location, mrDMD is able to identify a separation bubble in the vicinity of the shock train. The flow in and around the cavity remains largely undisturbed in this time bin as well.

(a) Snapshot 220/489, shows PCST after it moves slightly upstream

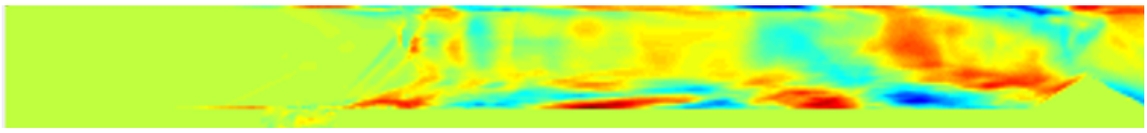

(b) DMD mode 20, still the mode that best identifies shocks near ramp

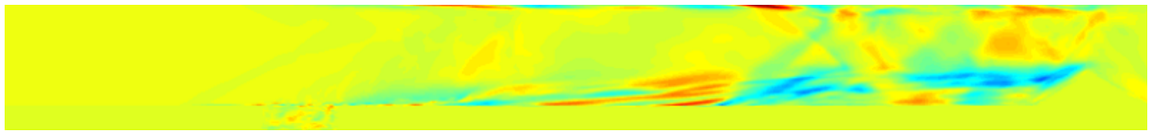

(c) mrDMD(3,2) mode 8, identifies shock train structures slightly upstream of ramp

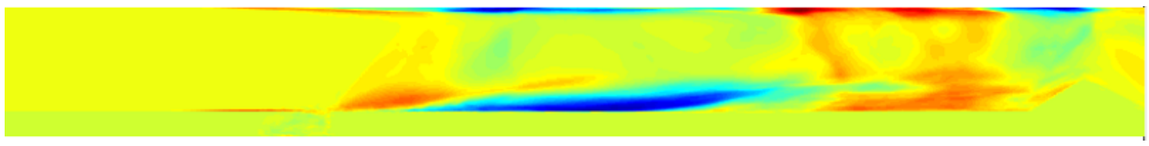

(d) mrDMD(3,2) mode 6, shows shock train and separation near front of shocks

Figure 21: Snapshot, DMD mode, and mrDMD mode comparison for level 3 bin 2

At the second time bin in the third level, mrDMD was again able to capture coherent structures that DMD failed to. mrDMD was able to capture both the shock train location and the coherent shape of the shocks, as shown in the rear portion of mode 6 from mrDMD(3,2). The large separation bubble shown on the bottom could be an indication of the significant upstream shock train movement that is occurring during this quarter of the snapshots.

During the third quarter of the snapshot series, the shock train and bottom wall separation bubble reach the cavity. Flow begins to spill into the cavity over the rear lip, significantly deflecting the shear layer and changing the structure of the PCST. There is significant movement of the shock waves near the rear cavity lip during this time bin.

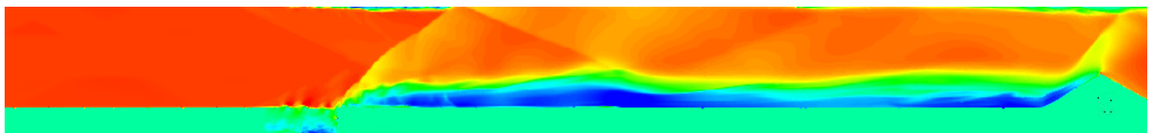

(a) Snapshot 350/489, shows PCST as it reaches cavity

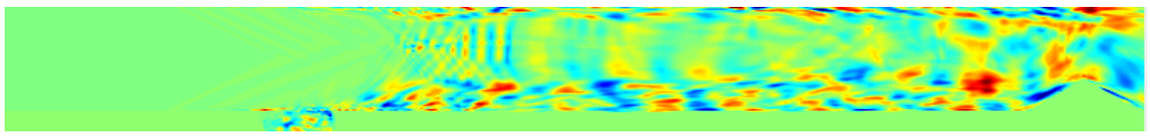

(b) DMD mode 71, mode that best identifies shock movement

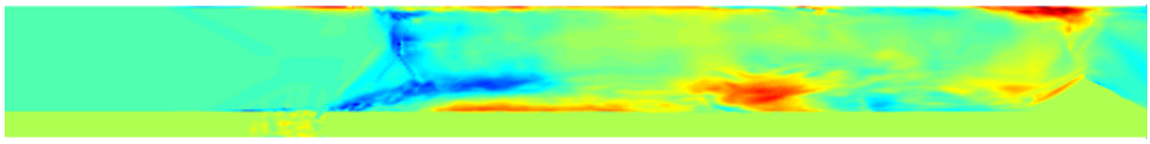

(c) mrDMD(3,3) mode 5, shows shock traces near cavity rear lip and shear layer deflection

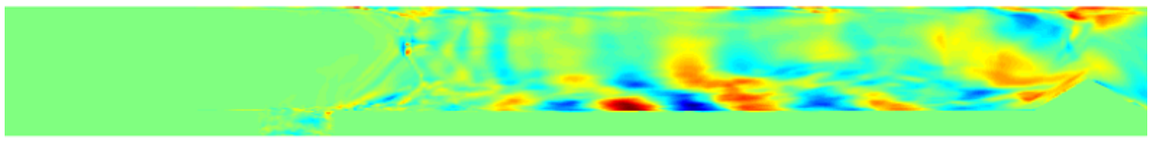

(d) mrDMD(3,3) mode 6, exhibits shock-stacking feature shown in DMD modes

Figure 22: Snapshot, DMD mode, and mrDMD mode comparison for level 3 bin 3

During the third time bin the PCST moves and changes to a more lambda like structure. This continual movement of the wave structure could be causing mrDMD(3,3) modes to exhibit the same shock-stacking phenomenon that the normal DMD modes exhibit, due to the implementation of the SVD on non-stationary data. The shock train movement dominates this portion of the snapshot series, and the stacking phenomenon occurring in both mrDMD(3,3) and DMD modes could be indicative that SVD based methods are ill-equipped to handle periods of shock movement and shape change. However, the stacking signature is less-profound in the mrDMD(3,3) modes than the DMD modes, but this could just be due to the time-localization to the third quarter of the time series.

In the fourth time bin, the shock train re-establishes itself with its new lambda like structure, and recedes downstream from the rear lip of the cavity to a more central location in the isolator. DMD was able to capture the final shock location, but the mode that depicted its location was associated with a significant decay rate. mrDMD was able to capture the shock train in its proper location, as well as identify its lambda structure, but the mrDMD(3,4) modes exhibit the same shock-stacking phenomenon as in mrDMD(3,3).

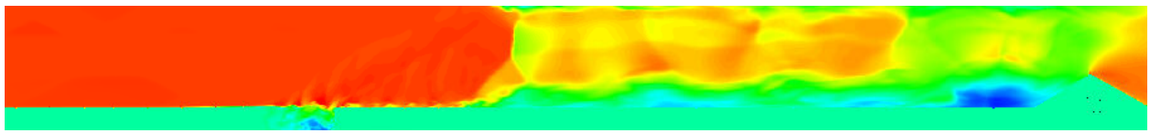

(a) Snapshot 444/489, shows PCST in its final location

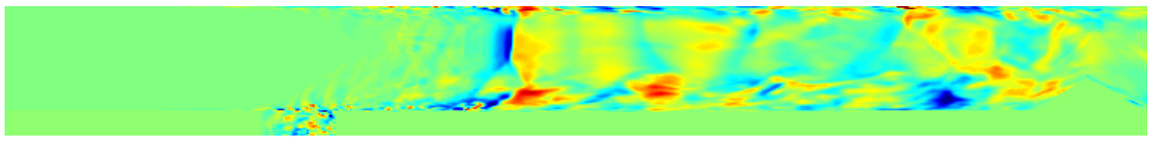

(b) DMD mode 175, mode that best identifies final PCST location

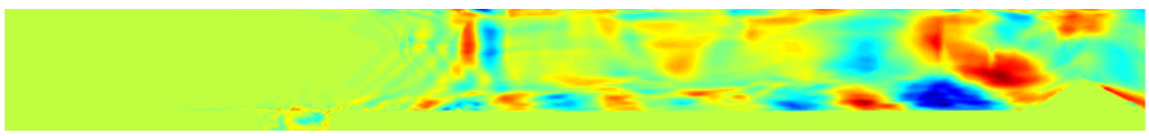

(c) mrDMD(3,4) mode 2, shows PCST final location and some shock-stacking

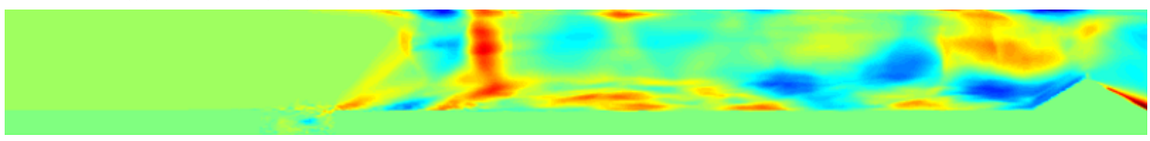

(d) mrDMD(3,4) mode 5, identifies final PCST structure

Figure 23: Snapshot, DMD mode, and mrDMD mode comparison for level 3 bin 3

Across all four time bins at the third level, mrDMD was able to identify coherent structures that DMD was either able to only resolve poorly, or failed to capture entirely. The modes from the periods of intense PCST movement and shape change ($j = 3, 4$), exhibit similar shock-stacking phenomena that the DMD modes do. This could be due to the difficulty the SVD has with characterizing translationally invariant structures in a low rank manner. Also since mrDMD is an unsupervised MRA method, only slow modes will be captured in each time bin. Un-captured 'fast' modes with higher magnitude eigenvalues could better represent the flow-field during these highly dynamical periods of shock movement.

3.4.3 mrDMD Level 4

At level four, the snapshots were divided into eight equal time bins. At this level of recursion, the movement of the PCST and development of separation is very clearly depicted. Many of the captured modes exhibit the shock-stacking pattern mentioned previously, but the major coherent structures in the flow-field are captured at their appropriate points in space and time, in a finer temporal resolution than at levels 1, 2, and 3. The clear identification of the dominant coherent structures as they evolve over time is indicative that higher level mrDMD analyses could better identify dynamical structures in non-stationary flow data, as demonstrated by the modes captured in the fourth level of the mrDMD analysis.

(a) mrDMD(4,1) mode 8

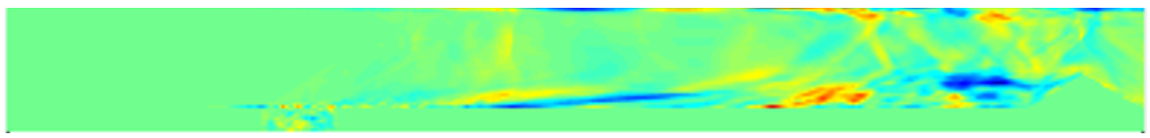

(b) mrDMD(4,2) mode 7

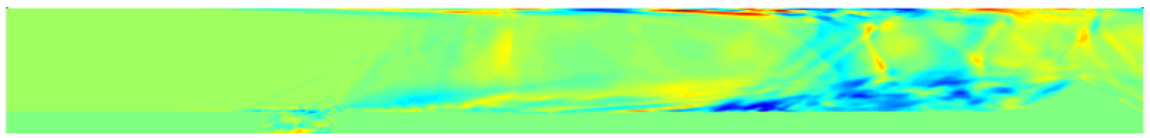

(c) mrDMD(4,3) mode 3

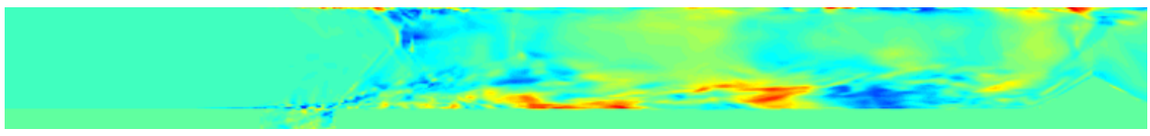

(d) mrDMD(4,5) mode 4

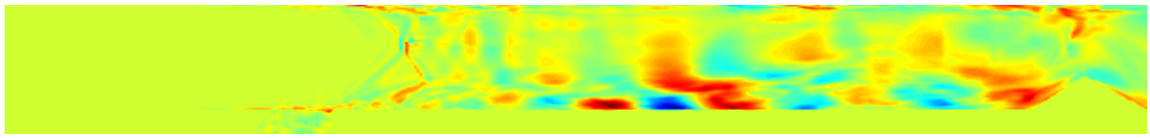

(e) mrDMD(4,6) mode 4

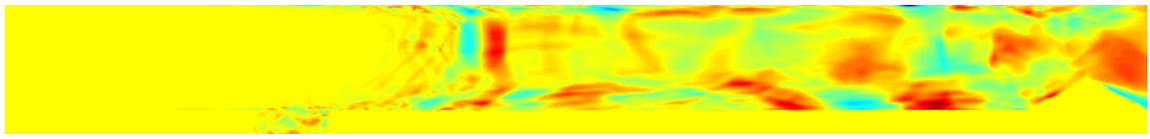

(f) mrDMD(4,7) mode 7

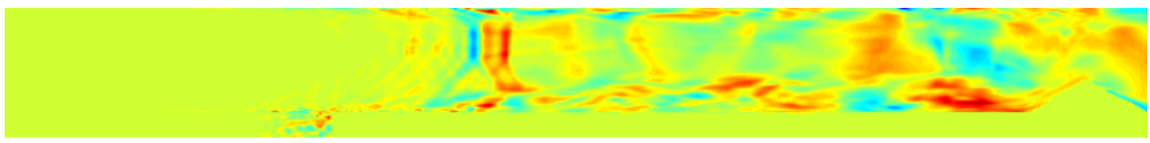

(g) mrDMD(4,8) mode 5

Figure 24: mrDMD mode comparison for level 4

As shown in 24, mrDMD was able to identify coherent structures and their time evolving nature in the isolator flow-field. At the highest level of recursion, the fine time-resolution allows for clear identification of PCST movement, separation development, and the changing of the PCST shape from purely oblique to a more lambda like structure. These features were not resolved in any meaningful way by DMD, and mrDMD clearly demonstrates its improved capability at handling non-stationary data at higher levels of recursion.

It should be noted no slow modes were retained for the fourth time bin at level four of the analysis, since all the continuous-time eigenvalues fell outside the threshold set by ρ as depicted in Fig 25. The shock-train experiences its most significant upstream movement in terms of physical distance during this eighth of the snapshots. This could possibly cause the DMD algorithm to attribute the isolator dynamics to modes with large magnitude eigenvalues, and consequentially impose more short-lived, high-frequency, and quickly decaying dynamics to the coherent structures in the flow-path.

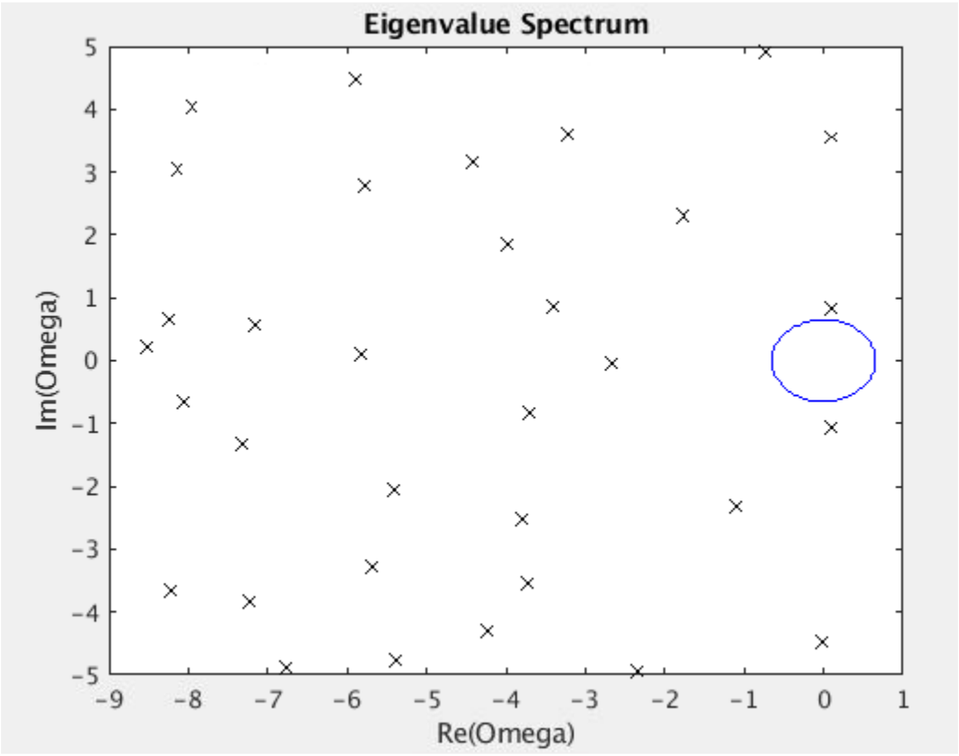

Figure 25: Continuous-time eigenvalue spectrum for mrDMD(4,4)

Chapter 4: Conclusions

Two data-driven modal decomposition techniques were used to analyze data from a LES simulation of a cavity controlled scramjet isolator undergoing unstart. The two methods that were employed were Dynamic Mode Decomposition (DMD) and its multi-resolution extension (mrDMD). The primary goal was to apply the modal decomposition techniques to identify the underlying coherent dynamical structures in the isolator during unstart. The secondary goal was to compare the results of the two methods, and determine the benefits mrDMD has over the base DMD method when it is applied to the statistically non-stationary case of scramjet unstart.

Before applying mrDMD to the non-stationary unstart flow-field, the algorithm was validated on the statistically stationary case of supersonic flow over a wall mounted turret. Since the flow is statistically stationary with no outlying events, mrDMD acted like the normal DMD algorithm, but with a Strouhal number filter at each level of recursion. The mrDMD method was able to accurately capture the density mean mode and dominant shock mode at the first level of recursion, where $\rho = St_{SBLI} \leq 0.3$. At higher levels of recursion, mrDMD was able to identify the turbulent boundary layer, rear shear layer, and separation regions that are present in the flow-field.

When applied to the unstart case, DMD was able to identify some gross flow features present in the isolator during the unstart event. Lower frequency DMD modes identified large bottom wall separation and shock train traces, while higher frequency modes identified cavity shear layer oscillations. DMD also completely failed to accurately capture the movement of the PCST as a coherent structure during unstart. Many of the captured DMD modes exhibited a 'shock-stacking' phenomena where many lambda-like shock structures were observed in close spatial proximity to each other near the rear lip of the cavity. This phenomena does not occur in the actual simulation, so this phenomena could be due to the application of a Singular Value Decomposition (SVD) based method to data that exhibits significant translational movement. It is also possible that the calculated DMD modes do not have much physical significance due to the data-driven nature of the method, so the results would need to be validated with other tools like FFT point probes.

The application of mrDMD to the unstart database yielded results that much more accurately depict the flow physics occurring in the isolator. The hierarchical nature of mrDMD allowed features like PCST movement, separation development, and shock cavity interactions to be identified starting at just the second level of analysis. As the level of recursion and temporal resolution increased, mrDMD was able to clearly identify the time-evolving location of coherent structures in the isolator, which was something that the base DMD method entirely failed to do. At level four, bin four of the mrDMD analysis no slow modes

were captured. This eighth of the snapshots corresponded to the period of most significant PCST movement, and the failure of mrDMD to capture low frequency dynamics could indicate the ability of mrDMD to identify periods of highly transient movement in a data set, in an entirely data driven manner. While the non-stationary effects of unstart are less pronounced in the smaller time bins of the higher analysis levels, the PCST still exhibits significant streamwise movement, which means the SVD based method might still be calculating physically irrelevant modes. Wavelet point probes might be pursued to determine if the dynamical modes calculated by mrDMD represent true underlying physics or not.

The two methods of DMD and mrDMD were both able to identify gross flow features present in the unstarting isolator. However, DMD failed to resolve the movement of these coherent structures through time, while mrDMD was able to capture structures in their correct spatio-temporal vicinities. This indicates that the time-windowing of snapshots and hierarchical time-frequency analysis used in the mrDMD method make it a more attractive modal decomposition technique for multi-scale and statistically non-stationary data sets. mrDMD still likely contains issues related to taking the SVD of non-stationary data, and future work to alleviate these issues could greatly improve the data-driven analysis of unstart simulations.

Appendix A: DMD COde

```
%Script to calculate DMD modes and Eigenvalues of Snapshot set.
clear all; close all; clc;

%%%Data Loading (Load S matrix from proper directory)
data = load('/mpidir_medusa/sullivan.1041/ugthesis/uvel_matsnaps/uvelsnaps.mat','S');
Xraw = data.S.var; %Declare Xraw variable
X1 = Xraw(:,1:end-1);
X2 = Xraw(:,2:end);

dt = .1; %Identify non-dimensional timestep

[U,S,V] = svd(X1,'econ');

Atil = U'*X2*V/S;
[W,D] = eig(Atil);
Lambda = diag(D);
Omega = log(Lambda)/(2*pi*dt);

Phi = X2*V/S*W;
x0 = X1(:,1);
b = Phi\x0;
abs_b_scaled = abs(b)/(max(abs(b)));
mag = abs(b);
freq = abs(imag(Omega));
modenum = 1:length(b);

DMDresults.Modes = Phi;
DMDresults.Lambda = Lambda; %Ritz Values
DMDresults.Omega = Omega;
DMDresults.b = b;
DMDresults.absmag = abs_b_scaled;

filename = input('Enter name for DMD results file\n','s')
save(filename,'DMDresults');
```

Appendix B: mrDMD Matlab Code

```
%For Loop Based mrDMD Algorithm, takes DMD formatted snapshots in and
outputs mrDMD results for user specified # of levels
clear all; close all; clc;

%%%Data Loading - Load S variable from 2D FV_snap_interpolate script
data1 = load('/mpidir_medusa/sullivan.1041/ugthesis/uvel_matsnaps/uvelsnaps.mat','S');
% data2 = load('rho_mrDMD_testsnaps_halfGrid_4000_4999.mat');

Xraw = data1.S.var;
dt = 0.1; %Time Step

%%%Algorithm Parameters (mrDMD = f(lvls,dt,cycles/period))
maxlev = 4; %Set number of mrDMD levels you want
maxbins = 2^(maxlev-1); %Bins per mrDMD level go as 2^(l-1)



%%% mrDMD Struct Initialization
%Create empty struct that is size(maxlev,maxbins)
mrDMD(maxlev,maxbins) = struct('Data',[]);

%%%mrDMD For Loop
for l=1:maxlev %level counter

    binlim=2^(l-1); %Set max bin limit for level of mrDMD
    datastep = size(Xraw,2)/(2^(l-1)); %Create datastep variable to increment
    datastep = floor(datastep); %Round integers down

    T = floor(size(Xraw,2)/l)*dt; %get time period for each level of mrDMD

    %RADIUS OF REMOVAL SELECTION
    rho = 7.96/T
    %rho = .3*l %radius set as St number*level

    for j=1:binlim %per bin DMD algorithm

        %Snapshot Allocation
        if j==1
            mrDMD(l,j).Data = Xraw(:,1:datastep);
```

```
else
    mrDMD(l,j).Data = Xraw(:,(j-1)*datastep+1:j*datastep);
end

%Add rho to struct for each bin
mrDMD(l,j).rho = rho;

%Perform DMD Algorithm
X = mrDMD(l,j).Data; %Set X equal to snapshot set for given bin
X1 = X(:,1:end-1); X2 = X(:,2:end);
[U,S,V] = svd(X1,'econ');

r = size(U,2);%Rank reduction variable

U = U(:,1:r); %Rank reduced SVD matrices
S = S(1:r,1:r);
V = V(:,1:r);

Atil = U'*X2*V/S;
[W,Lambda] = eig(Atil);
Lambda = diag(Lambda);
Omega = log(Lambda)/(2*pi*dt);
mrDMD(l,j).Omega = Omega; %Store data at given level,bin

%Calculate and Store DMD modes for jth bin
Phi = X2*V/S*W;
mrDMD(l,j).Phi = Phi;

%Calculate and Store mode amplitudes for jth bin
x0 = X1(:,1);
b = pinv(Phi)*x0;
mrDMD(l,j).b = b;

%OBTAIN SLOW MODES
ind = find(abs(Omega)<rho);

Phislow = Phi(:,ind);   %Slow DMD modes
Omegaslow = Omega(ind); %Slow DMD eigenvals
bslow = b(ind);
```

```
        %Store any results relating to slow modes for jth bin, lth level
        mrDMD(l,j).freq = abs(imag(Omegaslow));
        mrDMD(l,j).growthrate = real(Omegaslow);
        mrDMD(l,j).modenum = 1:length(bslow);
        mrDMD(l,j).mag = abs(bslow);
        mrDMD(l,j).Omegaslow = Omegaslow;
        mrDMD(l,j).Phislow = Phislow;
        mrDMD(l,j).bslow = b(ind);

        %Reconstruct Slow Mode dynamics
        mm1 = size(X,2);
        slowrank = length(ind);
        time_dyn = zeros(slowrank,mm1);
        time = (0:mm1-1)*dt;

        for iter=1:mm1
            time_dyn(:,iter) = bslow.*exp(Omegaslow*time(iter));
        end

        Xsub = zeros(size(Xraw)); %Placeholder variable

        Xdmdslow = Phislow*time_dyn; %Time solution of slow modes
        mrDMD(l,j).Xdmdslow = Xdmdslow; %Store slow mode soln

        %Subtract Slow Mode Time Dynamics from Full Data Set

        if j==1
        Xsub(:,1:datastep) = mrDMD(l,j).Xdmdslow;
        Xraw = Xraw - Xsub;
        else
        Xsub(:,(j-1)*datastep:j*datastep-1) = mrDMD(l,j).Xdmdslow;
        Xraw = Xraw - Xsub;
        end

    end
end

fprintf(1,'Saving\n')
filename = input('Enter name for DMD results file\n','s')
save(filename,'mrDMD','-v7.3')
```

References

[1] Matt Hall. Resolution and uncertainty in spectral decomposition. *First Break*, 24(12), 2006.

[2] J Nathan Kutz, Xing Fu, and Steven L Brunton. Multiresolution dynamic mode decomposition. *SIAM Journal on Applied Dynamical Systems*, 15(2):713–735, 2016.

[3] Andrew Joseph Crow. *Computational Uncertainty Quantification of Thermal Radiation in Supersonic Combustion Chambers.* PhD thesis, 2013.

[4] Kunihiko Taira, Steven L Brunton, Scott TM Dawson, Clarence W Rowley, Tim Colonius, Beverley J McKeon, Oliver T Schmidt, Stanislav Gordeyev, Vassilios Theofilis, and Lawrence S Ukeiley. Modal analysis of fluid flows: An overview. *Aiaa Journal*, 55(12):4013–4041, 2017.

[5] Seth M Hirsh, Kameron Decker Harris, J Nathan Kutz, and Bingni W Brunton. Centering data improves the dynamic mode decomposition. *SIAM Journal on Applied Dynamical Systems*, 19(3):1920–1955, 2020.

[6] Peter J Schmid. Dynamic mode decomposition of numerical and experimental data. *Journal of fluid mechanics*, 656:5–28, 2010.

[7] Jonathan H Tu, Clarence W Rowley, Dirk M Luchtenburg, Steven L Brunton, and J Nathan Kutz. On dynamic mode decomposition: Theory and applications. *arXiv preprint arXiv:1312.0041*, 2013.

[8] Clarence W Rowley, Igor Mezic, Shervin Bagheri, Philipp Schlatter, Dans Henningson, et al. Spectral analysis of nonlinear flows. *Journal of fluid mechanics*, 641(1):115–127, 2009.

[9] J Nathan Kutz, Steven L Brunton, Bingni W Brunton, and Joshua L Proctor. *Dynamic mode decomposition: data-driven modeling of complex systems*. SIAM, 2016.

[10] Steven L. Brunton and J. Nathan Kutz. *Fourier and Wavelet Transforms*, page 47–83. Cambridge University Press, 2019.

[11] Amara Graps. An introduction to wavelets. *IEEE computational science and engineering*, 2(2):50–61, 1995.

[12] Matan Gavish and David L Donoho. The optimal hard threshold for singular values is $\sqrt{\frac{4}{3}}$. *IEEE Transactions on Information Theory*, 60(8):5040–5053, 2014.

[13] Philip G Hill and Carl R Peterson. Mechanics and thermodynamics of propulsion. *Reading*, 1992.

[14] ET Curran, WH Heiser, and DT Pratt. Fluid phenomena in scramjet combustion systems. *Annual Review of Fluid Mechanics*, 28(1):323–360, 1996.

[15] Benjamin J Tatman, Robert D Rockwell, Chris P Goyne, James C McDaniel, and James M Donohue. Experimental study of vitiation effects on flameholding in a cavity flameholder. *Journal of Propulsion and Power*, 29(2):417–423, 2013.

[16] Logan Patrick Riley. *Unstart Phenomenology of a Dual-Mode Scramjet Subject to Time-Varying Fuel Input*. PhD thesis, The Ohio State University, 2019.

[17] Qiqi Wang, Karthik Duraisamy, Juan J Alonso, and Gianluca Iaccarino. Risk assessment of scramjet unstart using adjoint-based sampling methods. *AIAA journal*, 50(3):581–592, 2012.

[18] Leon Vanstone, Kelley E Hashemi, Joe Lingren, Maruthi R Akella, Noel T Clemens, Jeffrey Donbar, and Sivaram Gogineni. Closed-loop control of shock-train location in a combusting scramjet. *Journal of Propulsion and Power*, 34(3):660–667, 2018.

[19] Logan P Riley, Datta V Gaitonde, Mark A Hagenmaier, and Jeffrey M Donbar. Isolator dynamics during unstart of a dual-mode scramjet. *Journal of Propulsion and Power*, 34(6):1409–1427, 2018.

[20] Logan P Riley, Mark A Hagenmaier, Jeffrey M Donbar, and Datta V Gaitonde. A computational investigation of unstart in a dual-mode scramjet. In *54th AIAA Aerospace Sciences Meeting*, page 1901, 2016.

[21] JL Wagner, KB Yuceil, A Valdivia, NT Clemens, and DS Dolling. Experimental investigation of unstart in an inlet/isolator model in mach 5 flow. *AIAA journal*, 47(6):1528–1542, 2009.

[22] Hyungrok Do, Seong-kyun Im, M Godfrey Mungal, and Mark A Cappelli. The influence of boundary layers on supersonic inlet flow unstart induced by mass injection. *Experiments in Fluids*, 51(3):679–691, 2011.

[23] Robert Rockwell, Christopher P Goyne, Long Di, Zongli Lin, Robert Bakos, and Jeffrey M Donbar. Simulated shock train control using an all-coefficient adaptive control approach. In *AIAA Scitech 2019 Forum*, page 0126, 2019.

[24] Nathaniel J Alspach, Nathan J Webb, Dennis Omari, Datta V Gaitonde, and Mo Samimy. Joint computational/experimental analysis of a controlled supersonic cavity flow for scramjet applications. In *2018 Flow Control Conference*, page 4025, 2018.

[25] Steven L Brunton and J Nathan Kutz. *Data-driven science and engineering: Machine learning, dynamical systems, and control*. Cambridge University Press, 2019.

[26] Roger Penrose. A generalized inverse for matrices. In *Mathematical proceedings of the Cambridge philosophical society*, volume 51, pages 406–413. Cambridge University Press, 1955.

[27] Josh Alman and Virginia Vassilevska Williams. A refined laser method and faster matrix multiplication. In *Proceedings of the 2021 ACM-SIAM Symposium on Discrete Algorithms (SODA)*, pages 522–539. SIAM, 2021.

[28] Florimond Guéniat, Lionel Mathelin, and Luc R Pastur. A dynamic mode decomposition approach for large and arbitrarily sampled systems. *Physics of Fluids*, 27(2):025113, 2015.

[29] Mikala Malkus. An application of modal decomposition to supersonic flow over a wall-mounted turret, May 2020.